The path towards efficient wide band gap thin-film kesterite solar cells with transparent back contact for viable tandem application

Peer-reviewed author version

DOI: 10.1016/j.solmat.2020.110824
Handle: http://hdl.handle.net/1942/33169

The path towards efficient wide bandgap thin-film Kesterite solar cells with transparent back contact for viable tandem application

Samira Khelifi[a,b,*], Guy Brammertz[c,d,e], Léo Choubrac[f,h], Maria Batuk[g], Sheng Yang[a], Marc Meuris[c,d,e],Nicolas Barreau[f], Joke Hadermann[g], Henk Vrielinck[b], Dirk Poelman[b], Kristiaan Neyts[a], Bart Vermang[c,d,e], Johan Lauwaert[a]

[a] Department of Electronics and Information Systems (ELIS), Ghent University, iGhent Tower, Technology Park Zwijnaarde 126, 9052 Ghent, Belgium

[b] Department of Solid State Sciences, Ghent University, Krijgslaan S-1, 9000 Ghent, Belgium

[c] imec division IMOMEC-partner in Solliance, Wetenschapspark 1, 3590 Diepenbeek, Belgium

[d] Hasselt University-partner in Solliance, Martelarenlaan 42, 3500 Hasselt, Belgium

[e] EnergyVille, Thorpark 8320, 3600 Genk, Belgium

[f] Institut des matériaux Jean Rouxel (IMN), Université de Nantes, CNRS, 2 rue de la Houssiere, BP 32229, 44322 Nantes Cedex 03, France

[g] Electron Microscopy for Materials Science (EMAT), University of Antwerp, Groenenborgerlaan 171, 2020 Antwerp, Belgium.

[h] Department Structure and Dynamics of Energy Materials, Helmoltz-Zentrum Berlin für Materialien und Energie, Berlin 14109, Germany.

Abstract

Wide bandgap thin-film kesterite solar cell based on non-toxic and earth-abundant materials might be a suitable candidate as a top cell for tandem configuration in combination with crystalline silicon as a bottom solar cell. For this purpose and based on parameters we have extracted from electrical and optical characterization techniques of $Cu_2ZnGeSe_4$ absorbers and solar cells, a model has been developed to describe the kesterite top cell efficiency limitations and to investigate the different possible configurations with transparent back contact for four-terminal tandem solar cell application. Furthermore, we have studied the tandem solar cell performance in view of the bandgap and the transparency of the kesterite top cell and back contact engineering. Our detailed analysis shows that a kesterite top cell with efficiency > 14%, a bandgap in the range of 1.5-1.7 eV and transparency above 80% at the sub-bandgaps photons energies are required to achieve a tandem cell with higher efficiency than with a single silicon solar cell.

Keywords: kesterite thin-film solar cell; $Cu_2ZnGeSe_4$; secondary/ternary phases, wide bandgap absorbers; efficiency limitations; four-terminal tandem solar cell; c-Si solar cell

1. Introduction

Kesterite materials have been widely investigated as potential absorber layers for thin-film solar cell technology with a record efficiency of 12.6% reported for CZTSSe based devices [1]. The bandgap of these absorbers can be tuned either by varying the S/Se content or by partially replacing tin (Sn) atoms by silicon (Si) or germanium (Ge) atoms. The development of wide-bandgap kesterite solar cells based on abundant and low-cost materials might be beneficial for tandem solar cell applications, if used as a top cell with the existing high efficiency crystalline silicon solar cells in a four-terminal configuration.

However, since most of the earth abundant materials have strong absorption and poor electronic properties due to their chemical and structural defects, further development of both absorber material and device architecture are required to achieve high-efficiency devices.

Germanium incorporation in CZTSSe kesterite based solar cells has been studied before and device efficiencies up to 9-12 % have been reported with bandgaps in the range of 1.2-1.1 eV [2,3]. Also, kesterite solar cells with a bandgap of 1.4-1.5 eV were fabricated with pure Ge substitution [4,6]. However, the efficiency of Ge based kesterite solar cells is still below the record efficiency obtained in CZTSe cells. Thus, further and significant improvement of both absorber materials and device structure have to evolve to achieve high-efficiency solar cells based on these compounds.

The current challenge with kesterite based solar cells is the growth of the kesterite phase without secondary phases which are known to limit the solar cell performance. The most commonly reported secondary phases (binary and ternary) are Zn(S)Se, $Cu(S)Se_2$, $Sn(S)Se_2$, $Cu_2Sn(S)Se_3$ [7-10] and has been reported even in devices with high efficiency. Their effect on the solar cell performance strongly depends on their position in the kesterite film and their electrical and optical properties. They could form at the front, in the bulk and at the back side of the thin film, therefore it is important to track down their location in the film and understand the conditions of their formation during the film growth in order to avoid or minimize their effect.

However, despite the availability of several wet chemical etchants to remove the secondary phases, only the ones located at or near the surface of the film can be etched away during the device preparation.

The use of earth abundant and low toxic material as a top cell on a crystalline Si bottom cell in a tandem configuration is an alternative layout suggested to boost the solar cell efficiency and

reduce the production costs. In tandem structure, photocurrent matching is one of the requirements that should be considered in the design of series-connected tandem solar cells, which is usually obtained by adapting the thickness of the top cell and the bandgaps of both top-cell and bottom-cell. In a four-terminal mechanically stacked tandem structure, current matching is not necessary, since the two cells are independently connected. However, because of the mechanical stacking approach, a top-cell with transparent electrodes and good transparency at long wavelengths is mandatory.

In this work, $Cu_2ZnGeSe_4$ (CZGSe) absorbers and ZnO/CdS/$Cu_2ZnGeSe_4$/Mo/Glass solar cells with an optical bandgap of E_g ~ 1.5eV and an efficiency up to 7% are studied using various electro-optical characterization techniques to investigate the device performance. Furthermore, we present a model based on realistic parameters extracted from the measurements to discuss in detail the efficiency limitation in these wide band gap materials.

In addition, numerical simulations are used to determine some of the cell requirements and the best configuration for the kesterite based solar cell with transparent back contact if to be used as a top cell on a c-Si bottom cell in a four-terminal tandem structure.

2. Experimental

2.1. Device preparation

The solar cells were prepared by DC-sputtering of Cu and Zn layers and e-beam evaporation of Ge layer on 5×5 cm^2 Soda-Lime Glass (SLG)/SiON/Mo substrate. The SiON barrier layer was used to inhibit the diffusion of Na and other impurities from the glass into the absorber. The precursor layers were then selenized at 470 °C in a 10 % H_2Se atmosphere for 15 min. The absorbers were etched in a HCl solution with a concentration 12wt.% and at a temperature 80°C for 15-20min to remove ZnSe secondary phases from the surface of the CZGSe absorber.

For the solar cell preparation, a thin *n*-type CdS buffer layer was deposited using chemical bath deposition, followed by RF-sputtering of *i*-ZnO (120 nm) and Al doped ZnO (350 nm) layers. For the top contact, a 50 nm Ni - 1 μm Al finger grid pattern was evaporated through a shadow mask. Cells with an area about 0.5 cm^2 were isolated by needle scribing. More details about the cells preparation can be found in Ref [4-5].

2.2 Device characterization

X-ray diffraction (XRD) was performed on thin film absorbers deposited on glass and on complete solar cells to study the structural properties of the films. The XRD patterns of the

films were performed on a Bruker D8 Discover equipped with a LynxEye silicon strip detector in the Bragg-Brentano configuration with Cu Kα radiation.

Fourier transform infrared spectroscopy was carried out using a Brucker Hyperion 2000 microscope coupled to a Bruker Vertex 80v. The measurements were recorded in reflection using the microscope under near normal incidence conditions to estimate the thickness of the films from the interference fringes. The IR absorbance was performed using the spectrometer to investigate the vibrational modes of the kesterite and any other phases which may be produced during the growth of the films.

Transmission/Reflection spectra were measured on CZGSe absorber deposited on Quartz using a Varian Cary 500 UV/Vis spectrometer.

The mobility of the *p*-type CZGSe films deposited on glass was determined from AC Hall measurements in the VanderPauw configuration.

Capacitance voltage (*C-V*) and admittance spectroscopy *C-f-T* (AS) were carried out using a HP 4192 A LF impedance analyzer in the frequency range 10^2-10^7Hz. The doping density in the CZGSe absorbers was calculated from the *C-V* measurements, while the admittance spectroscopy technique allows us to identify and analyze the defects in these devices [11]. Temperature dependent measurement *C-f-T* and *J-V-T* were performed using a cold finger cryostat mounted on a nitrogen source.

The microstructure of the cells and the film morphology was further investigated using transmission electron microscopy (TEM) on samples prepared using the focused ion beam (FIB) technique, on a Be support. Prior to the sample preparation, a Pt/carbon layer is deposited on the films to protect the surface layer. High angle annular dark field scanning transmission electron microscopy (HAADF-STEM) images and energy dispersive X-ray (EDX) maps were acquired using a FEI Tecnai Osiris microscope equipped with a Super-X detector and operated at 200 kV.

The data were recorded using probes with convergence semi-angles in the 21– 25 mrad range (with a probe size of about 1 Å) and the EDX maps were generated from the intensity of the Cu–K, In–L, Ga–K, Se–K, Cd–L, S–K, Zn–K, O–K, C–K, and Mo–K lines.

3. Results and Discussion

3.1 Electro-optical characterization

Fig. 1 shows the XRD measurements performed on a bare CZGSe absorber and the complete solar cell. The kesterite phase is formed in both cases with good crystallinity in a tetragonal

lattice with a = 5.606Å and c = 11.042Å. In Fig. (1a), XRD peaks related to ZnSe phases can clearly be seen in the XRD patterns of the CZGSe absorbers grown on glass before the HCl chemical etch. These peaks are no longer detectable in the finished devices (Fig. (1b)), as the absorbers underwent hot wet-chemical etch before the chemical bath deposition of the CdS buffer layer.

The optical bandgap of the absorbers was deduced from the tauc-plot [12] of the absorption coefficient and has values between 1.45-1.49 eV in these CZGSe based solar cells as plotted in Fig. 2.

The CZGSe film thickness as determined from the interference fringes has values between 1.4 and 1.7 μm. A refractive index of 2.92 was used for the calculation of the film thickness, as estimated from the Moss equation [13]:

$$E_g n^4 = k \qquad (1)$$

where E_g is the bandgap of the material and k is a constant with values 95-108 eV.

The absorption coefficient α was calculated from the measured transmission and reflectance of the films using UV-Vis spectroscopy as [14]

$$\alpha(\lambda) = \frac{1}{d} ln \left[\frac{1-R(\lambda)}{T(\lambda)}\right] \qquad (2)$$

The doping density in these cells is quite low ($<10^{15}$ cm^{-3}) plausibly caused by the use of the SiON barrier layer which inhibits diffusion of Na into the absorber layer. In their work on the beneficial incorporation of Ge into CZTSe absorber, Giraldo et al., [15] have demonstrated that during the reactive annealing there was a strong reaction between Ge and Na, which controls the doping density of the absorber.

The role of Na was well investigated in Cu(In,Ga)Se_2 based solar cells [16] and its beneficial effect has also been reported in kesterite solar cells. It was shown that adding Na during the film growth either by diffusion from the SLG substrate or by using a Na precursor layer, enhances the grain growth of the film [17] and increases the *p*-type doping of the absorber and the open-circuit voltage (V_{oc}) [18,19]. Note that the *p*-type concentration measured by the Hall measurements on these CZGSe films deposited directly on glass was quite high ~10^{18} cm^{-3} and we assigned this to a high diffusion of Na from the soda lime glass into the absorber. This leads us to conclude that using controlled Na precursor layers might be the best way to incorporate Na in these absorbers and use its beneficial effects. The average value of hole mobility measured in the films was 2.3 cm^2/V.s. Also, it is worth considering that the mobility measured by Hall-effect measurements is commonly limited by defect states and a high potential energy

barrier at the grain boundaries where scattering of carriers plays an important role in the polycrystalline films.

Admittance spectroscopy (AS) and current-voltage measurements under different temperature and illumination (*J-V-T*) were performed to get more information about defects and recombination mechanisms governing the performance of these devices.

The admittance spectroscopy spectra *C-f-T* were converted into density of defect states using the theory and the analysis discussed in [20] to reduce the noise of the admittance spectra:

$$N_t(E_\omega) = -\frac{(V_{bi}-V)^2}{w[qV_{bi}-E_{Fn\infty}]}\frac{dC}{d\omega}\frac{w}{kT} \qquad (3)$$

Where N_t is the defect density, w is the depletion width, V_{bi} the built-in voltage, V the applied voltage, q the elementary charge, $E_{Fn\infty}$ a Fermi energy level, C the capacitance and ω the angular frequency.

Admittance spectroscopy measurements unveil the presence of two defects: a shallow one around 100-150 meV and a deep defect with an energy level around 280 meV.

Fig. 3 shows the distribution of the defect energy levels as measured from admittance spectroscopy and approximated by a Gaussian distribution of deep states [11]. Although this technique cannot distinguish between acceptor and donor defect levels, it allows to determine the energy distribution within the bandgap of the material with sufficient reliability. It was reported that the *p*-type conductivity in kesterite films is determined by both V_{Cu} and Cu_{Zn} antisites defects. According to the calculation of Chen et al. [21], these defects are formed in Kesterite under *Cu*-poor and *Zn*-rich growth conditions, with a shallow level at 0.01-0.02 eV for the V_{Cu} defect and a deeper level around 0.11-0.150 eV for Cu_{Zn}. Although the latter is in good agreement with the defect level measured here at 150 meV, a barrier-like signal, as it was reported in chalcogenide based solar cells on Mo/SLG substrates cannot be excluded [22,23]. The first-principles calculation of defect formation in CZGSe semiconductors done by Nishihara et al. [24] shows that *Cu* vacancies can be easily formed under *Cu*-poor condition in this compound, which makes it a *p*-type absorber for thin-film solar cells and antisite defects like Cu_{Zn} can hardly be formed under these conditions. The average composition of the CZGSe films as deduced from TEM-EDX measurements is [Cu]/([Zn]+[Ge])= 0.9 and [Zn]/[Ge]= 1.03. The films are *Cu*-poor with *Zn*/*Ge* ratio nearly equal to 1 therefore the doping is most likely controlled by the presence of *Cu* vacancies V_{Cu}.

Current-voltage measurement performed at different temperatures is displayed in Fig. 4. This measurement technique provides an insight into recombination processes limiting the device performance, especially the open-circuit voltage V_{oc}. The diode current under dark is given by:

$$J = J_s\left[e^{\left(\frac{qV}{nkT}\right)} - 1\right] \qquad (4)$$

Where n is the diode ideality factor and kT/q the thermal voltage. J_s is the saturation current and is expressed as:

$$J_s = J_0 e^{\frac{E_a}{nkT}} \qquad (5)$$

Where E_a is an activation energy or a barrier governing recombination under dark condition and J_0 is a prefactor weakly temperature dependent.

Under open-circuit condition $J = J_{sc}$ (J_{sc} the short-circuit current), V_{oc} is then given by

$$V_{oc} = \frac{E_a}{kT} - \frac{nkT}{q} ln\left(\frac{J_0}{J_{sc}}\right) \qquad (6)$$

From Eqs. (5) and (6) one can see that a decrease in E_a increases the dark current and lowers V_{oc}. When the activation energy E_a is equal to the absorber bandgap E_g, bulk recombination is dominant. When interface recombination is dominant, the activation energy E_a is lower than E_g and represents a barrier at the interface. It is worth mentioning here that E_a lower than E_g could be due to the presence of secondary phases in the absorber or band gap fluctuation. In this case the main recombination loss takes place at the area with lower energy and a higher saturation current at the secondary phase areas may occur as well.

The extrapolation of the V_{oc} to 0 K using Eq. (6) gives an activation energy of 995 ± 24.5 meV which is below the CZGSe absorber bandgap energy in these devices. Also, current-voltage curves at different temperatures displayed a strong roll-over at low temperature as shown in Fig. 5, which may be caused by the presence of a barrier limiting the device performance.

3.2 Films morphology

Fig. 6 shows the HAADF-STEM images of the CZGSe solar cell as well as individual elemental EDX maps and a Cu/Zn/Se/Ge/Cd/Mo mixed map. The sample consists of a CZGSe layer of a thickness about 1.0-1.7 μm with grain sizes about 200-400 nm. The structure and composition of the CZGSe absorber is not uniform, as one can see in the maps. There are regions of admixture phases which are attributed to inclusions of ZnSe at the top of the absorber layer, $Cu_{2-x}Se$ phase which is present at the grain boundaries and at the interface with the Mo back contact and and Cu_2GeSe_3 at the back of the CZGSe absorber. The Cu_2GeSe_3 phase is rather thick and has a thickness between 120 and 160 nm. The average of Cu:Zn:Ge:Se atomic ratios taken on 38 spectra measured at different locations in the film, is found to be 27.4:13.2:12.8:49.6 giving a composition of $Cu_{1.95(0.07)}Zn_{1.06(0.06)}Ge_{1.02(0.05)}Se_{3.97(0.11)}$. Note that

close to the Mo back contact, other elements like Si, N, O and C are also detected and their presence is related to the SiON barrier layer at the back contact.

FTIR spectroscopy was performed in absorbance on lifted-off CZGSe absorbers and is presented in Fig. 7. The IR active modes in the kesterite lattice have B and E symmetry [25,26]. They are also Raman active and their labelling in Fig. 7 is based on earlier results reported using Raman spectroscopy [27], where the IR active modes appear with weak intensity. Note that the ZnSe secondary phases on the top of the CZGSe were not detected in the absorbers after the HCl chemical etch. However, the vibrational mode at 215 cm^{-1} which corresponds to the (LO) mode of Cu_2GeSe_3 phase [28] is detected which confirms the presence of the ternary phase at the back of the CZGSe absorber, in accordance with the results of the TEM analysis. Raman spectroscopy has been widely used to determine the kesterite and secondary phases in earth abundant based solar cells but to the best of our knowledge these are the first reported results on FTIR performed on kesterite materials showing the IR active vibrational modes and the presence of the Cu_2GeSe_3 ternary phase in these CZGSe wide band gap devices.

4. Modelling and simulations

In the first part of this section, we present a model which is developed to explain the CZGSe solar cell performance using SCAPS software [29]. In the second part, the parameters limiting the cell performance are analyzed and discussed. Then, a model for a transparent back contact (TBC) based on optimized cell parameters which can be used for tandem applications is presented and compared with the standard configuration of a cell with Mo/SLG back contact. Finally, a model for the kesterite-Si tandem structure is presented and discussed in depth as a function of the kesterite top cell bandgap and transparency.

The starting parameters used in the simulations were obtained by a set of electrical and optical characterization techniques performed on the $Cu_2ZnGeSe_4$ (CZGSe) thin-film absorber and the complete solar cell as given in section 2.2.

The enhancement of kesterite solar cells performance through back contact optimization has been predominantly related to the presence and the control of a $Mo(S,Se)_2$ layer reported in most thin-film solar cells grown on Mo-coated soda-lime glass, such as CIGSe [30], CZTSe [31]. The presence of this layer determines the selective electrical back contact for the absorber layer.

However, in these devices the interface between the CZGSe absorber and Mo back contact is rather complicated and contains several inclusions, but the main feature is the formation of a

big inclusion of crystalline Cu_2GeSe_3 phase at the bottom of the absorber. Therefore, the selective back contact is defined by the presence of this ternary phase.

Cu_2GeSe_3 is reported to be a ternary *p*-type semiconductor with a direct band gap of 0.78-0.94 eV[32,33]. In the work of Endo et al [34], the Hall mobility and concentration measured at room temperature are 0.5 $cm^2/V.s$ and $10^{19} cm^{-3}$, respectively and are quite dependent on the annealing temperature of the samples.

In our calculation, a Cu_2GeSe_3 ternary phase with a thickness of 120-150 nm as determined by TEM measurements was included in the model with the material properties given in Table. 1. Reflectance loss on the kesterite cell surface was considered in all calculations and no internal reflections at the top/bottom cell or optical parasitic loss were included. All the other parameters used in the simulations are summarized in Table 1.

4.1. Model for a CZGSe based solar cell with $\eta \sim 7\%$

In virtue of the complicated structure of thin-film solar cells, there is no straightforward method that can be used to model all the measurements data. However, one can always start with a partial model which can describe a specific behavior or a measurement but has a marginal effect on the other measurements and consequently helps to understand or describe the complete cell behavior. In our case, we started by a first set of parameters to describe the doping profile (from capacitance-voltage measurements) and current-voltage measurements under dark and illumination conditions.

The *p*-type doping in the CZGSe absorber was introduced as a shallow acceptor level at 0.02 eV above the valance band with low capture cross section, considering the presence of V_{Cu} as discussed in section 2. In this case, the defect acts as dopant but does not contribute to the recombination. The deep defect with an activation energy of 280 meV was introduced as an acceptor level with a concentration in the range of 10^{15} cm^{-3} and a hole capture cross section $\sigma_p = 9\times10^{-16}\,cm^2$ as deduced from the Arrhenius plot shown in the inset of Fig. 3. There is no information about the charge states that could form at the interface between the CdS buffer layer and the CZGSe absorber layer, due to secondary phases or any other species which might be introduced after the chemical etching treatment. Thus, recombination at the CdS/CZGSe interface is added assuming charge-free SRH recombination.

The current-voltage and capacitance-voltage curves were calculated using our model for the CZGSe solar cell with 7% efficiency. A good agreement between the simulations and the measurements is obtained as shown in Fig. 8 and 9 and the solar cell outputs given in Table S1 in supplementary information. The non-uniform doping profile was reproduced by assuming an

exponentially graded doping profile in the absorber which gives quite a decent fit with the measurement as can be seen in Fig. 9(b).

As stated before, the presence of the ternary phase Cu_2GeSe_3 will define the selective back contact with the Mo layer. Mo has a low metal work function of 4.9 eV therefore a Schottky barrier is expected at the back $CuGe_2Se_3$/contact. However, the presence of this ternary phase with a band gap (0.9 eV) lower than the band gap of the CZGSe absorber (1.5 eV) creates a large blocking barrier for the majority carriers (holes) as illustrated in the energy band diagram in Fig. 10. The effect of these barriers on the solar cell performance is discussed in the next section. Also, to our knowledge, this is the first time the effect of a ternary phase formed at the back surface of a kesterite absorber, not directly related to the Mo back contact layer, is taken into account in numerical modelling based on experimental observations.

According to the measurements and simulations, the solar cell performance limitations are caused by several parameters such as deep defect assisted recombination, low doping and carrier mobility in the absorber, a blocking barrier and parasitic effects due to high series resistance and low shunt resistance. Each of these parameters will be studied and discussed in more detail in the next section.

4.2 Optimization of solar cell parameters

In this section, we analyse the effect of each loss mechanism on the performance of the CZGSe based solar cells in order to optimize the cell parameters and increase the solar cell efficiency.

4.2.1 Effect of doping and deep defects in the CZGSe absorber

In these compounds, we found that high diffusion of Na from the SLG into the CZGSe absorber was detrimental for the solar cell performance, while using a barrier layer such as SiON inhibits diffusion of Na into the absorber. Consequently, this leads to low doping in the absorber and decreases the open-circuit voltage.

Based on admittance spectroscopy, a deep acceptor defect with a level around 229 meV was reported in CZTSe solar cells deposited on alkali-free borosilicate glass, which became shallower with sodium incorporation [19]. The defect agrees well with the one measured in our devices around 280 meV and could be related to an insufficient amount of Na in the absorber. The role of Na on the enhancement of the device performance is still under debate and it seems more likely that its beneficial effect is related to the removal or redistribution of native point defects in the absorber, as has also been suggested for CIGSe and CZTSe based solar cells [19,36].

The solar cell efficiency was calculated as function of the concentration of the deep acceptor trap at 280 meV and the results are displayed on Fig. 11(a). It shows that the presence of this deep defect has a strong effect on the solar cell efficiency, when its concentration is higher than 10^{15} cm^{-3}. However, the effect is less severe if we could consider that the deep defect becomes shallower with an energy level at 100 meV above the valence band. To explain the effect of this defect on the cell behavior, we calculate the internal recombination in the absorber at a voltage V=0.5 V, in order to compare the recombination around the open-circuit voltage. As shown in Fig. 11(b), the loss in the device performance is caused by an increase of recombination in the absorber when the defect level gets deeper in the bandgap and/or is present with concentration $N_{\mathrm{Tdefect}} > 10^{15}\mathrm{cm}^{-3}$.

Therefore, due to the strong reaction between Ge and Na from the SLG during the CZGSe absorber deposition, we suggest the use of thin Na precursor layers during the absorber growth as the best strategy to control the diffusion of Na into the absorber and increase both the doping and the open-circuit voltage. For tandem applications, this may be the only practical way to optimize the doping in the absorber since growing absorbers directly on a transparent back contact without soda-lime glass may lead to very low doping in the CZGSe layer and accordingly to poor electrical properties of the absorber.

We showed in the experimental part that the doping in these devices was quite low and below 10^{15} cm^{-3}. There are several downsides of low doping in the absorber layer which directly influence the open-circuit voltage. First, it leads to low built-in voltage and consequently to low open-circuit voltage. Moreover, an absorber layer with low doping increases the space charge region and the recombination rate in it. Which further reduces the open-circuit voltage. Simulated open-circuit voltage and efficiency versus the doping N_A in the CZGSe absorber shows that the optimum value of the *p*-type doping in these devices should be in the range $10^{15} \leq N_A \leq 10^{17}$ cm^{-3} (see Fig. S1 in supplementary information).

Since the hole mobility is expected to vary with the *p*-type doping of the absorber and a lower doping density should lead to a higher hole mobility, the device performance can be improved with absorbers having higher grain quality. The efficiency is plotted as a function of doping and hole carrier mobility in the CZGSe absorber (Fig. S2 in supplementary information), showing that an increase in device efficiency of 1 to 2% absolute can be achieved with doping density $10^{16} \leq N_A \leq 10^{17}$ cm^{-3} and hole mobility values higher than 40 $cm^2/V.s$. While the doping of the absorber can be increased by using alkali precursor layers, improvement of the bulk grain quality in order to increase the mobility of the films is still a big challenge, knowing that the highest hole mobility measured in kesterite materials till now was about 39.7 $cm^2/V.s$ with a

doping of $p = 2\times10^{17}$cm^{-3} in CZTSe films grown at substrate temperature of 400°C [37]. Note that a mobility of minority carriers "electrons" of about 100 cm^2/V.s was considered in our calculations consistent with the values of 70-140 cm^2/V.s reported in *p*-type kesterite absorbers [38,39].

4.2.2 Effect of series and shunt resistance

Another major factor limiting the CZGSe cell performance is the parasitic series and shunt resistances. The high series resistance reported in most kesterite solar cells was mainly attributed to the presence of a blocking back contact barrier induced by the presence of a thick $Mo(S,Se)_2$ layer at the back contact [40,41], and/or secondary phases near the heterojunction such as Zn(S,Se), which act as interface recombination centers [42]. On the other hand, low shunt resistance was related to the presence of voids and secondary phases in the absorber. In these CZGSe cells, the parasitic resistances are possibly produced by several factors including the presence of secondary phases in the absorber (ZnSe), ($Cu_{2-x}S$) and voids as revealed by the TEM measurements. Moreover, the presence of a Cu_2GeSe_3 ternary phase at back of the CZGSe absorber creates a barrier for the majority carriers and a non-ideal Schottky contact and may increase the parasitic resistance effect.

Till now all the record efficiencies in kesterite based solar cells were reported for devices with series resistance below 2 Ω.cm^2 [43,1]. To analyse the effect of high series resistance and low shunt resistance on the device performance, the efficiency of the CZGSe cell is calculated as a function of the parasitic resistances. We found that the optimum device performance is reached for series resistance below 2 Ω.cm^2 and shunt resistance above 800 Ω.cm^2 (see Fig. S3 in supplementary information).

4.2.3 Effect of band alignment and interface states at CdS/CZGSe

The presence of interface states and the type of conduction band alignment (conduction band offset) at the CdS/CZGSe interface may be both responsible for the large open-circuit deficit commonly observed in kesterite devices. In the case of CdS/CZGSe with n^+p structure (with low absorber doping $N_D >> N_A$), electrons are majority carriers at the interface and the interface recombination is governed by holes of the absorber. Note that, there are two distinguished paths for the recombination at the interface depending whether the heterojunction is of type (I) or of type (II) [44]:

- In a type (I) heterojunction where $\Delta E_c > 0$, with a spike like conduction band offset (CBO, and electrons recombine with holes of the absorber.

- In a type (II) heterojunction where $\Delta E_c < 0$, with a cliff-like conduction band offset (CBO), electrons in the buffer recombine with holes in the absorber.

The properties of the interface are evaluated by the interface recombination velocity S_i and the number of interface states as follow:

$$S_i = N_i \sigma_{n,p} v_{th_{n,p}} \quad (7)$$

Where N_i is the concentration of the interface states, $\sigma_{n,p}$ is the thermal capture cross section of electrons/holes and $v_{th_{n,p}}$ is the thermal velocity of electrons/holes.

The interface recombination current is given by

$$J_i = qS_i(p - p_0) \quad (8)$$

with $p - p_0$ the excess of minority carriers at the absorber side.

In Fig. 12, V_{oc} and η are plotted as a function of the interface recombination velocity S_i and the conduction band offset ΔE_c. A device efficiency in a range of 8-10 % is obtained for conduction band offset in the range $-0.1 < \Delta E_c < 0.3$ eV and interface recombination velocity $S_i \leq 10^4$ cm/s. In the same range of ΔE_c, the open-circuit voltage reaches maximum values above 600 meV and is quite independent of the interface quality for positive band offset ΔE_c where inversion layer occurs at the interface. In case of negative band offset ΔE_c the open-circuit voltage decreases with higher interface velocities. As one can deduce from Eq. (6), the decrease in V_{oc} for cliff-like band alignment is directly related to a decrease of the barrier at the interface.

These findings reveal that the limitation of the device performance and especially the V_{oc} deficit are only slightly affected by the band alignment ΔE_c and the quality of the buffer/absorber interface in these wide band gap kesterite devices. Hence, the open-circuit deficit is most likely due to an internal barrier in the CZGSe absorber layer created by secondary (or ternary) phase segregation with low band gap inside the absorber such as the Cu_2GeSe_3 phase.

4.2.4 Effect of blocking barrier

The non-idealities observed in thin-film solar cell characteristics have been reported to be instigated by non-ohmic back contact [45,46]. In CIGSe and kesterite, where molybdenum is commonly used as back contact material, device performance limitations were attributed to the formation of Mo(S,Se) layer at the interface due to the reaction of absorber elements (e.g., S or Se) with Mo contact. Replacing Mo by another material contact is advisable but finding an alternative back contact with high metal work function and stable ohmic contact for kesterite solar cells is quite challenging especially for an absorber material with wide band gap and low *p*-type doping density.

The hole barrier height is defined by the difference between the Fermi energy level and the valence band edge as:

$$\phi_b = E_{F_p} - E_V \qquad (9)$$

In Fig. 13 the barrier for holes ϕ_b is calculated using Eq. (9) as a function of the doping of the layer in contact with the Mo layer. Thus, the doping is varied in the Cu_2GeSe_3 ternary phase present between the CZGSe absorber layer and the Mo contact. The height of the barrier calculated at the Mo contact is constant and equal to $\phi_0 = 130$ meV, which is in accordance with the value deduced from AS measurements and assigned to a barrier signal response at the back contact. On the other hand, the barrier for holes induced by the presence of Cu_2GeSe_3 is quite dependent on the doping and decreases when the *p*-type doping in this layer increases. This is because the valence band edge E_v shift up when increasing the doping in the Cu_2GeSe_3 layer. Note that the value calculated for a high doping concentration is very close to the activation energy E_a deduced from the $V_{oc}(T)$ plot extrapolated to 0 K in Fig. 4. The simulations corroborate that the high open-circuit voltage deficit recorded in the devices is engendered to a large extent by an internal hole blocking barrier created by the presence of a Cu_2GeSe_3 ternary phase at the back of the CZGSe absorber. The open-circuit deficit is calculated assuming different back contact type (Schottky or Ohmic), with and without the presence of the ternary phase and the results are presented in Fig.14. It is readily apparent that a high V_{oc} deficit is recorded in the presence of the Cu_2GeSe_3 ternary phase independent of whether the back contact is Schottky- or Ohmic-type. While without the ternary phase the deficit is reduced from 900 meV to 600 meV with a device efficiency in a range 14-15%.

4.3. CZGSe solar cells on a transparent back contact (TBC) for tandem applications

As stated before, a conducting back contact with good transparency is indispensable for the CZGSe cell when it is to be used as a top-cell in tandem applications. In this section, different structure configurations are tested and discussed based on the model developed and using optimized parameters of the doping in the CZGSe absorber and the parasitic resistances. The optimized parameters are cited in Table 1.

4.3.1 Molybdenum (Mo) back contact versus Transparent Back Contact (TBC)

Fig. 15 displays the open-circuit voltage deficit and efficiency of a CZGSe solar cell with two different back contact configurations: CZGSe on transparent back contact (TBC) and CZGSe on TBC using molybdenum oxide (MoO_x) as an intermediate layer. The calculations were performed using the realistic cell parameters extracted from measurements and using the

optimized parameters for doping density in the absorber and parasitic resistances given in Table 1, without the presence of Cu_2GeSe_3 layer. Practically, the removal of the ternary phase at the back surface of the absorber layer could be achievable by exfoliation process to remove the Mo back contact as it has been successfully realized for CIGSe and CZTSe solar cells [47,48], followed by chemical etching to remove the ternary phase or any other phases or elemental residues [49,50]. Another advantage of the exfoliation process is that it allows the deposition of the kesterite cell on a transparent back contact at low temperature avoiding the degradation of the latter during a high temperature deposition and selenization processes of the kesterite absorber.

However, when using a transparent back contact the main loss in the device performance will be provoked by a drop in the V_{oc}, which is a consequence of the low metal work function of the TBC leading to non-ideal band alignment with the CZGSe absorber. Moreover, most of the conductive transparent oxides used in solar cell technology have a low metal work function in the range of 4.7-4.9 eV [51] and may not be suitable as back contact materials in CZGSe devices. In this case, the use of an intermediate layer such as MoO_3 is recommended to overcome this problem. As one can see in Fig. 15, the V_{oc} deficit in the solar cell can be reduced when using an intermediate layer with high band gap such as MoO_3. For the record, MoO_3 has already been used as interfacial layer between TBC (ITO) and the $Cu(In,Ga)Se_2$ absorber in a superstrate configuration [52] and between $Cu_2ZnSnSe_4$ and Mo contact to improve the back contact properties, and further as a primary back contact in kesterite solar cells [53,54]. Furthermore, the thickness of the MoO_x layer needs to be optimized to reduce the light absorption loss in this layer and maintain good transparency of the top cell for tandem application.

4.4 Kesterite-Si Tandem Structure

To calculate the efficiency of a four terminal tandem solar cell, we used the CZGSe with the optimized parameters obtained in section 3.2 as a top cell on a Si bottom cell. For the bottom Si solar cell, a SCAPS model which was developed for a PERL Si cell with 25 % efficiency is used [55]. In the model we consider a n^+pp^+ structure with a wafer thickness (absorber layer) of 300 µm and a ZnS/MgF_2 double anti-reflection layer as described in [56]. The light trapping was included using the Lambertian scattering scheme [57-59]. Then, the effect of the top cell bandgap and long-wavelengths transmission is studied and discussed for various cell structures.

4.4.1 Effect of the top cell bandgap

The bandgap of the CZGSe absorbers prepared in this work with pure Ge substitution was about 1.5 eV, which is not high enough for efficient tandem applications. Not only a wide bandgap material is mandatory but also good transparency at long wavelengths together with a high cell efficiency are required for the top cell to be used on a Si bottom cell in tandem applications. Therefore, it is essential to know the efficiency limitations in these devices. For this purpose, the efficiency of the kesterite solar cell was calculated as a function of the absorber bandgap. Theoretical studies have shown that the bandgap of $Cu_2ZnSn_{1-x}Ge_xSe_4$ and $Cu_2ZnSn_{1-x}Si_xSe_4$ alloys as function of the *x* composition for both 'Ge' and 'Si' substitute [60] varies from 1 to 1.5eV and from 1 to 2.3eV respectively.

We started from a device efficiency of up to 10% for the standard kesterite cell with the presence of the Cu_2GeSe_3 phase at the back of the absorber and up to 15% for a cell without the ternary phase and an intermediate MoO_x layer between the absorber and the TBC back contact, as suggested in section 4.3.1, and then varied the bandgap of the absorber from 1.45 eV to 2.3 eV. In this way, the effect of a wide range of bandgaps either based on Ge/Sn or Si/Sn compounds are analyzed using realistic device parameters.

Indubitably, varying the bandgap also induces a change in the band alignment at the conduction and valence bands. Shu et al. [60] reported in their first-principles calculations study, that the substitution of Sn by Ge or Si does not significantly change the valence band maximum (VBM) energies, because they consist of Se 4*p* and Cu 3*d* orbitals. Thus, we assumed that changes in the band alignment occur predominantly in the conduction band and that the conduction band offset (CBO) varies between 0.2 and -0.65 eV in the range of the bandgaps given above. We used the absorption coefficient as measured for the CZGSe absorber and we varied the bandgap accordingly. The calculated efficiency of the top cell versus the absorber bandgap and the conduction band offset (CBO) is displayed in Fig. 16 for a standard cell and a cell with a MoO_x layer, respectively. The efficiency drops in these devices from 10% to 3% when the bandgap of the absorber increases from 1.45 eV to 2.3 eV due to the large negative cliffs. Nevertheless, device efficiencies higher than 8 % can still be maintained for absorber bandgaps $1.4 \leq E_g \leq 1.8$ eV and $-0.15\text{eV} \leq \text{CBO} \leq 0.2$ eV. The advantage of an exfoliation and the use of MoO_x intermediate layer in case of a TBC contact can clearly be seen in the band gap range $1.40 \leq E_g \leq 1.85$ eV and conduction band offset range $-0.20\text{eV} \leq \text{CBO} \leq 0.25\text{eV}$, where device efficiency up to 16% could be achieved.

4.4.2 Effect of the top cell bandgap and transmission at long wavelengths

In a tandem configuration, the light incident on the bottom cell is limited by the bandgap of the top cell since only photons with energies $E<E_g$ will reach the bottom cell. In the ideal situation, this requires a top cell with sub-bandgap transmission T=1, which is not possible in practice due to parasitic absorption losses.

The efficiency of the tandem solar cell is assessed by varying both the bandgap, the conduction band offset and the transparency of the top cell, for a standard top cell and for a cell with MoO_x. Note that the efficiency decreases when the bandgap increases, as it was shown previously and T≠0 for sub-bandgap wavelengths. The results are given in Fig. 17. In the case of a standard cell with higher bandgap and transparency higher than 80%, the efficiency is still not enough to retrieve the loss from the filtered Si-bottom cell. On the other hand, using a top cell with an efficiency between 15% and 13 %, a bandgap between 1.55 and 1.7 eV and T>85% already leads to an increase in the efficiency of 0.4-1.5 %, compared to the Si-bottom cell alone.

4.4.3 Example of a $Cu_2ZnGeSe_4$/Si tandem cell

We use the specifications obtained in the previous sections for the thin film top cell to evaluate the performance of the four terminal tandem cell. The Si bottom cell efficiency was calculated assuming a CZGSe cell with a bandgap E_g=1.5 eV on top of it which is optically active and absorbs a significant fraction of the light. Another essential parameter which is required for the design of the top cell in a tandem configuration is the thickness of the CZGSe absorber. The thickness should be optimized in a way to maintain a good transparency and at the same time minimize the absorption loss by the top cell. at the same time. Fig. 18 presents the calculated *J-V* and *EQE* for the CZGSe/MoO_x-top cell (η=17%) with a thinner absorber d = 1μm and the Si-bottom cell being filtered by the top cell (η=9.4%). The efficiency of the four-terminal tandem cell in this case is 25.6% and an increase of 1.4% is obtained compared to the Si PERL cell alone.

Conclusions

The highest efficiency reported in CZGSe with pure Ge is above 7% and there is still room for further enhancement regarding the device performance. At this stage, there are several cell parameters limiting the device efficiency which are quite below the parameters found in state of art CIGSe solar cells, such as the low doping of the absorber and the low mobility. However, the main loss in the device performance is caused by the presence of a Cu_2GeSe_3 ternary phase at the back of the absorber surface which creates an internal hole blocking barrier and increase

the V_{oc} deficit. Device efficiency in a range of 14-15% can be reached if the ternary phase is removed, which could be realized by exfoliation of the back contact and a using a selective chemical etching.

Kesterite thin-film solar cells might be a good candidate as a top cell in combination with a Si crystalline bottom cell in a four-terminal tandem structure. However, the kesterite device performance is still below the requirements regarding the absorber bandgap, efficiency and transparency. The bandgap of $Cu_2ZnSn_{1-x}Ge_xSe_4$ and $Cu_2ZnSn_{1-x}Si_xSe_4$ alloys can easily be tuned by Si or Ge substitution in a range of 1 to 2.3 eV which is compatible with the recommended bandgaps for the top cell in tandem structure when used with a Si bottom cell. However, increasing the bandgap will be at the cost of decreasing the device efficiency in cells based on these alloys. Hence, further developments should be focused on cell layer engineering especially at the front and back contact to improve the device performance. Our calculations show that a cell with an efficiency above 14%, bandgaps in a range of 1.5-1.7 eV and a transparency above 85% at long wavelengths are required to reach an efficiency gain of about 1-2% compared to the record Si cell efficiency of 25%.

Acknowledgments

The authors would like to acknowledge the SWInG project financed by the European Union's Horizon 2020 research and innovation programme under grant agreement No 640868 and the Research Foundation Flanders-Hercules Foundation (FWO-Vlaanderen, project No AUGE/13/16:FT-IMAGER).

References

1 W. Wang, M.T. Winkler, O. Gunawan O, T. Gokmen, T.K. Todorov, Y. Zhu, D.B. Mitzi, Device Characteristics of CZTSe Thin-Film Solar Cells with 12.6% Efficiency. *Adv Energy Mater* 4 (7) (2014) 1301465.

2 C.J. Hages, S. Levcenco, C.K. Miskin, et al., Improved performance of Ge-alloyed CZTGeSSe thin-films solar cells through control of elemental losses. Prog. Photovolt Res. Appl. 23 (3) 2015 376-384.

3 S. Kim, K.M. Kim, H. Tampo, et al., Improvement of voltage deficit of Ge-incorporated kesterite solar cell with 12.3% conversion efficiency. Appl. Phys. Express. 9 (10) (2016) 102301.

[4] Sahayaraj S, Brammertz G, Vermang B, et al., Optoelectronic properties of thin film $Cu_2ZnGeSe_4$ solar cells. Sol. Energy Mater. Sol. Cells. 171 (2017) 136-141.

[5] L. Choubrac, G. Brammertz, et al., 7.6% CZGSe solar cells thanks to optimized CdS chemical bath deposition, Phys. Status. Solidi. A. 215 (2018) 1800043.

[6] E. Garcia-Llamas, J.M. Merino, R. Serna, et al., Wide band-gap tuning $Cu_2ZnSn_{1-x}Ge_xS_4$ single crystals: Optical and vibrational properties. Sol. Energy Mater. Sol. Cells. 158 (2) (2016) 147-153.

[7] Nirav Vora, Jeffrey Blackburn, Ingrid Repins, et al., Phase identification and control of thin films deposited by co-evaporation of elemental Cu, Zn, Sn, and Se. J. Vac. Sci. Technol. A 30(5) (2012) 051201.

[8] P. A. Fernandes, P.M.P. Salomé, A.F. da Cunha, Precursors' order effect on the properties of sulfurized Cu_2ZnSnS_4 thin films. Semicond. Sci. Technol. 24 (2009) 105013.

[9] C. Platzer-Björkman, J. Scragg, H. Flammersberger, T. Kubart, M. Edoff,. Influence of precursor sulfur content on film formation and compositional changes in Cu_2ZnSnS_4 films and solar cells. Sol. Energy. Mater. Sol. Cells. 98 (2012) 110-117.

[10] Wan-Ching Hsu, Ingrid Repins, Carolyn Beall et al,. Growth mechanisms of co-evaporated kesterite: a comparison of Cu-rich and Zn-rich composition paths. Prog. Photovolt. Res. Appl. 22 (2014) 35-43.

[11] S. Khelifi, K. Decock, J. Lauwaert, et al,. Investigation of defects by admittance spectroscopy measurements in poly (3-hexylthiophene):(6,6)-phenyl C61-butyric acid methyl ester organic solar cells degraded under air exposure. J. Appl. Phys. 110 (9) (2011) 094509

[12] B.D. Viezbicke, S. Patel, B.E. Davis, et al., Evaluation of the Tauc method for optical absorption edge determination ZnO thin fims as a model system. Phy. Status. Solidi. B. 252(8) (2015) 1700-1710.

[13] N.M. Ravindra, P. Ganapathy, J. Choi, Energy gap-refractive index relations in semiconductors. Infra. Phys. Tech. 50 (1) (2007) 21-29.

[14] Pankove IV. Optical Processes semiconductors. *Dover Inc*. 1975; New York.

[15] S. Giraldo, M. Neuschitzer, M. Placidi, et al., $Cu_2ZnSnSe_4$-based Solar Cells With Efficiency Exceeding 10% by Adding Superficial Ge Nanolayer: The Interaction Between Ge and Na. IEEE. J. Photovolt. 6 (3) (2016) 754-759.

[16] T. Nakada, D. Iga, H. Ohbo, et al. Effects of Sodium on $Cu(In,Ga)Se_2$ Based Thin Films and Solar Cells. Jpn. J. Appl. Phys. 36 (2) (1997) 732-737.

[17] C.M. Sutter-Fella, J.A. Stückelber, H. Hagendorfert, et al., Sodium Assisted Sintering of Chalcogenides and its Application to Solution Processed $Cu_2ZnSn(S,S_2)$ Thin Film Solar cells. Chem. Mater. 26 (3) (2014) 1420-1425.

[18] L. De la Cueva, Y. Sánchez, L. Calvo-Barrio, et al., Sulfurization of co-evaporated $Cu_2ZnSnSe_4$ thin film solar cells: The role of Na. Sol. Energy Mater. Sol. Cells. 186 (2018) 115-123.

[19] J.V. Li, D. Kuciauskas, M.R. Young, et al., Effects of sodium incorportation in Co-evaporated $Cu_2ZnSnSe_4$ thin-film solar cells. Appl. Phys. Lett. 102 (16) (2013)163905.

[20] Koen Decock, Samira Khelifi, Marc Burgelman, An automated method to reduce noise of admittance spectra allowing assessment of a large number of complicated spectra, 26th European Photovoltaic Solar Energy Conference and Exhibition, EU PVSEC Proceedings. (2011) 2922-2925

[21] S. Chen, A. Walsh, X.G. Gong, et al., Classification of lattice defects in the Kesterite Cu_2ZnSnS_4 and $Cu_2ZnSnSe_4$ earth-abundant solar cell absorbers. Adv. Mater. 25 (11) (2013) 1522-1539.

[22] T. Eisenbarth, T. Unold, R. Caballero, et al., Interpretation of admittance, capacitance-voltage and current-voltage signatures in $Cu(In,Ga)Se_2$ thin film solar cells. J. Appl. Phys. 107 (3) (2010) 034509.

[23] J. Lauwaert, S. Khelifi, K. Decock, et al., Signature of a back contact barrier in DLTS spectra. J. Appl. Phys. 109 (6) (2011) 063721.

[24] H. Nishihara, T. Maeda, T. Wada, First-principles study of defect formation in a photovoltaics semiconductor $Cu_2ZnGeSe_4$. Jpn. J. Appl. Phys. 57(2S2) (2018) 02CE06.

[25] M. Himmrich and H . Haeuseler, Far infrared studies on stannite and wurtzstannite type compounds , Spectrochimica Acta. 47A (7) (1991) 933-942.

[26] Tanju Gürel, Cem Sevik, Tahir Çağn, Characterization of vibrational and mechanical properties of quaternary compounds Cu_2ZnSnS_4 and $Cu_2ZnSnSe_4$ in kesterite an stannite structures, Phys. Rev B (84) (2011) 205201.

[27] M. Guc, S. Levcenko, V. Izquierdo-Roca, X. Fontané, E. Arushanov, A. Pérez-Rodríguez, Polarized Raman scattering analysis of Cu2ZnSnSe4 and Cu2ZnGeSe4 nsingle crystals, J. Appl.Phys. 114 (19) (2013) 193514.

[28] V. Riede, N. Sharif, H. Neumann, H. Sobotta, M.S. Omar, B.R. Pamplin, Infrared Lattice Vibrations in Cu_2GeSe_3, Cryst. Res. Technol. 22(8) (1987) 1089-1093.

[29] M. Burgelman, K. Decock, S. Khelifi, et al. Advanced electrical simulation of thin film solar cells. Thin Solid Films. 535 (2013) 296-301.

[30] D. Abou-Ras, G. Kostorz, D. Bremaud, et al., Formation and characterisation of $MoSe_2$ for Cu(In,Ga)Se_2 based solar cells. Thin Solid Films. 480-481 (2005) 433-438.

[31] B. Shin, Y. Zhu, N.A. Bojarczuk, et al., Control of an interfacial $MoSe_2$ layer in $Cu_2ZnSnSe_4$ thin film solar cells: 8.9 % power conversion efficiency with a TiN diffusion barrier. Appl. Phys. Lett. 101(5) (2012) 053903.

[32] Masaru Morihana, Tsuyoshi Maeda, Issei Yamauchi, Takahiro Wada, Crystallographic and optical properties of narrow band gap Cu_2GeSe_3 and $Cu_2(Sn_{1-x}Ge_x)Se_3$ solid solution, Japanese Journal of Applied Physics. 53, 05FW06 (2014)

[33] Otfried Madelung, Semiconductors: Data Handbook, Springer-Verlag Berlin Heidelberg, 3rd edition (2004).

[34] Saburo Endo, Ichiro Sudo, Taizo Irie, On the electrical and thermal properties of ternary chalcogenide $A_2^I B^{IV} \chi_2$, $A^I B^V \chi_2$ and $A_3^I B^V \chi_4$ ($A^I = Cu$; $B^{IV} = Ge, Sn$; $B^V = Sb$; $\chi = S, Se, Te$), Japanese Journal of Applied Physics, 10 (2) (1971) 218-223.

[35] H. Simchi, B.E. McCandless, T. Meng, et al., Characterization of reactively sputtered molybdenum oxide films for solar cell application. J. Appl. Phys. 114 (1) (2013) 013503.

[36] A. Rockett, The effect of Na in polycrystalline and epitaxial single-crystal $CuIn_{1-x}Ga_xSe_2$. Thin Solid Films. 480-481 (2005) 2-7.

[37] R.A. Wibowo, E.S. Lee, B. Munir, et al., Pulsed laser desposition of quaternary $Cu_2ZnSnSe_4$ thin films. Phys. Status. Solidi a. 204 (10) (2007) 3373-3379.

[38] H. Hempel, A. Redinger, I. Repins, et al., Intragrain charge transport in kesterite thin films-Limits arising from carrier localization, J. Appl. Phys. 120(17) (2016) 175302.

[39] G.W. Guglietta, K.R. Choudhury, et al., Employing time-resolved terahertz spectroscopy to analyze carrier dynamics in thin-film $Cu_2ZnSn(S,Se)_4$ absorber layers. Appl. Phys. Lett. 104(25) (2014) 253901.

[40] K. Wang, O. Gunawan, T. Torodov, et al., Thermally evaporated Cu_2ZnSnS_4 solar cells. Appl. Phys. Lett. 97(14) (2010) 143508.

[41] D.B. Mitzi, O. Gunawan, T.K. Torodov, et al., The path towards a high-performance solution-processed kesterite solar cell, Sol. Energy Mater. Sol Cells. 95(6) (2011) 1421-1436.

[42] J.J. Wätjen, J. Engman, M. Edoff, et al. Direct evidence of current blocking by ZnSe in $Cu_2ZnSnSe_4$ solar cells. Appl. Phys. Lett. 100(17) (2012) 173510.

[43] S. Bag S, O. Gunawan, T. Gokmen, et al., Low band gap liquid-processed CZTSe solar cell with 10.1% efficiency. Energy Environ Sci. 5 (2012) 7060.

[44] Alex Niemegeers, Marc Burgelman, Alexis De Vos, On the CdS/CuInSe2 conduction band discontinuity, Applied Physics Letters. 67(6) (1995) 843-845.

[45] Alex Niemeegeers, Marc Burgelman, Effects of Au/CdTe back contact on *IV* and *CV* characteristics of Au/CdTe/CdS/TCO solar cells, Journal of Applied Physics. 81(6) (1997) 2881-2886.

[46] P. Nollet, M. Burgelman, S. Degrave, The back contact influence on characteristics of CdTe/CdS solar cells, Thin Solid Films 361-362 (2000) 293-297.

[47] Yasuhiro Abe, Takashi Minemoto, Hideyuki Takakura, Origin of crossover in current density-voltage characteristics of Cu(In,Ga)Se2 thin film solar cell fabricated using lift-off process, Japanese Journal of Applied Physics. 50 (2011) 040201.

[48] Kong Fai Tai, Oki Gunawan Kuwahara, Shi Chen, Subodh Gautam Mhaisalkar, Cheng Hon Alfred Huan, David B. Mitzi, Insights from physical and electrical characterization of devices and exfoliation films, Advanced Energy Materials. 6 (2016) 1501609.

[49] Priscilla D. Antunez, Douglas M. Bishop, Yun Seog Lee, Tayfun Gokmen, Oki Gunawan, Talia S. Gershon, Teodor K. Todorov, Saurabh Singh, Richard Haight, Back contact engineering for increased performance in Kesterite solar cells, Advanced Energy Materials. 7 (2017) 1602585.

[50] Kasra Sardashti, Evgueni Chagarov, Priscilla D. Antunez,Talia S. Gershon, Scott T. Ueda, Tayfun Gokmen, Douglas Bishop, Richard Haight, Andrew C. Kummel, Nanoscale Characterization of Back Surfaces and Interfaces in Thin Film Kesterite Solar Cells, ACS Applied Materials & Interfaces. 9 (2017) 17024−17033.

[51] A. Klein, C. Körber, A. Wachau, et al., Transparent conducting oxides for photovoltaics: Manipulation of fermi level, work function and energy band alignment, Materials. 3(11) (2010) 4892-4914.

[52] H. Simchi, J.K Larsen, K. Kim, et al., Improved Performance of Ultrathin Cu(In,Ga)Se_2 Solar Cells With a Backwall Superstrate Configuration. IEEE J Photovolt. 4(6) (2014) 1630-1635.

[53] S. Lopez-Marino, M. Espindola-Rodriguez, Y. Sanchez, et al., The importance of back contact modification in $Cu_2ZnSnSe_4$ solar cells: The role of a thin MoO_2 layer. Nano Energy. 26 (2016) 708-721

[54] J. Park, J. Huang, K. Sun, et al., The effect of thermal evaporated MoO_3 intermediate layer as primary back contact for kesterite Cu_2ZnSnS_4 solar cells. Thin Solid Films. 648 (2018) 39-45.

[55] J. Zhao J, Al. Wang, M. Green, 24.5% Efficiency Silicon PERT Cells on MCZ Substrates and 24.7% Efficiency PERL cells on FZ Substrates. Prog. Photovolt. Res. Appl. 7(6) (1999) 471-474.

[56] Jianhua Zhao, Aihua Wang, Pietro P. Altermatt et al., 24% Efficient perl silicon solar cell : Recent improvements in high efficiency silicon cell research. Sol. Energy Mater. Sol. Cells. 41(42) (1996) 87-99.

[57] S. Khelifi, M. Burgelman, J. Verschraegen, et al., Impurity photovoltaic effect in GaAs solar cell with two deep impurity levels. Sol. Energy Mater. Sol. Cells. 92(12) (2008) 1559-1565.

[58] S. Khelifi, J. Verschraegen, M. Burgelman, et al. Numerical simulation of impurity photovoltaic effect in silicon solar cells. Ren Energy. 33(2) (2008) 293-298.

[59] M. Green, The path to 25% silicon solar cells efficiency: History of the silicon cell evolution, Prog. Photovolt. Res Appl. 17(3) (2009) 183-189.

[60] Q. Shu, J.H. Yang, S. Chen, et al. $Cu_2Zn(Sn,Ge)Se_4$ and $Cu_2Zn(Sn,Si)Se_4$ alloys as photovoltaic materials: Structural and electronic properties. Phys. Rev. B. 87(11) (2013) 115208.

Tables

Table 1 Parameters used in the simulations at standard solar cell test conditions. The values marked by $^{(*)}$ are the optimized parameters after the simulations.

Parameter	*ZnO*	*CdS*	*CZGSe*	Cu_2GeSe_3[32-34]	MoO_x[35]
d(μm)	0.150	0.045	1.4	0.125	0.04
E_g (eV)	3.3	2.4	1.5	0.9	2.85
χ (eV)	4.4	4.2	4.41	4.13	2.6
μ_n (cm^2/V.s)	100	100	100	20	20
μ_p (cm^2/V.s)	25	25	2	2	20
N_d (cm^{-3})	10^{18}	1×10^{17}	-	-	-
N_A (cm^{-3})	-	-	$2\times10^{14}/10^{16(*)}$	10^{19}	10^{17}
ϕ_b (eV)	0.130				
R_s (Ω.cm^2)	$5/1.5^{(*)}$				
R_{sh} (Ω.cm^2)	$370/900^{(*)}$				

Captions

Figures

Figure 1 XRD patterns measured on CZGSe absorber film deposited on Glass (a) and on the CZGSe solar cell (b).

Figure 2 Optical bandgap of CZGSe absorber extracted from the Tauc plot of the absorption coefficient.

Figure 3 Defect density in CZGSe solar cell calculated from admittance spectroscopy measurements (*C-f-T*). Symbols: measurements, solid lines: curve Fit using Gaussian distribution for defect states. The inset shows the Arrhenius plot of the defect at 280 meV.

Figure 4 Temperature dependence of V_{oc} measured in CZGSe cell and extrapolated at 0K giving an activation energy $E = 995 \pm 24.5$ meV.

Figure 5 Current-voltage measurements of CZGSe cell at different temperatures.

Figure 6 HAADF-STEM image, separate EDX maps and combined EDX map of the solar cell. Secondary phases regions are indicated by arrows: ZnSe (blue arrows), Cu_2GeSe_3 (pink arrows) and $Cu_{2-x}Se$ (yellow arrows).

Figure 7 FTIR measured in absorbance on lifted-off CZGSe absorbers. The IR active modes of the kesterite lattice having E and B symmetry are shown. The labelling is based on early reported Raman peaks [27].

Figure 8 Dark and light current-voltage curves. Symbols: measurements, Solid lines: simulations.

Figure 9 (a) Mott-Schottky plot from capacitance voltage (*C-V*) at frequency $f = 10^5$Hz and (b) Doping profile extracted from the Mott-Schottky plot. Symbols: measurements, Solid lines: simulations.

Figure 10 Band energy diagram at the CZGSe back surface/Mo back contact showing the contact barrier ϕ_0 at the Mo contact and the formation of a blocking barrier ϕ_b induced by the presence of Cu_2GeSe_3 ternary phase.

Figure 11 (a) Effect of deep trap concentration $N_{Tdefect}$ on the solar cell efficiency. The case of the defect E_t = 280 meV shifting to a shallow level E_t =100 meV is considered. (b) The Calculated recombination $R(x)$ in the absorber for E_t = 100 meV and E_t = 280 meV with different defect concentrations $N_{Tdefect}$= $10^{14}cm^{-3}$ and $N_{Tdefect}$= $5\times10^{15}cm^{-3}$.

Figure 12 Efficiency (η) and open-circuit voltage (V_{oc}) versus CdS/CZGSe interface recombination velocity and conduction band offset (ΔE_c).

Figure 13 Barrier height calculated at the Mo contact (ϕ_0) and at Cu_2GeSe_3/CZGSe back surface (ϕ_b) as a function of the *p*-type doping in the Cu_2GeSe_3 ternary phase.

Figure 14 Open-circuit deficit calculated for different back contact-type with and without Cu_2GeSe_3 ternary phase.

Figure 15 Open-circuit deficit and efficiency calculated for different back contact configurations.

Figure 16 Efficiency of the kesterite top cell versus its bandgap and the conduction band offset (ΔE_c) for a standard cell and cell with MoO_x.

Figure 17 Efficiency of the tandem cell as function of the top cell bandgap and transmission.

Figure 18 External quantum efficiency (EQE) of the CZGSe/MoO_x top cell and the Si filtered bottom cell.

Figure 1(a)

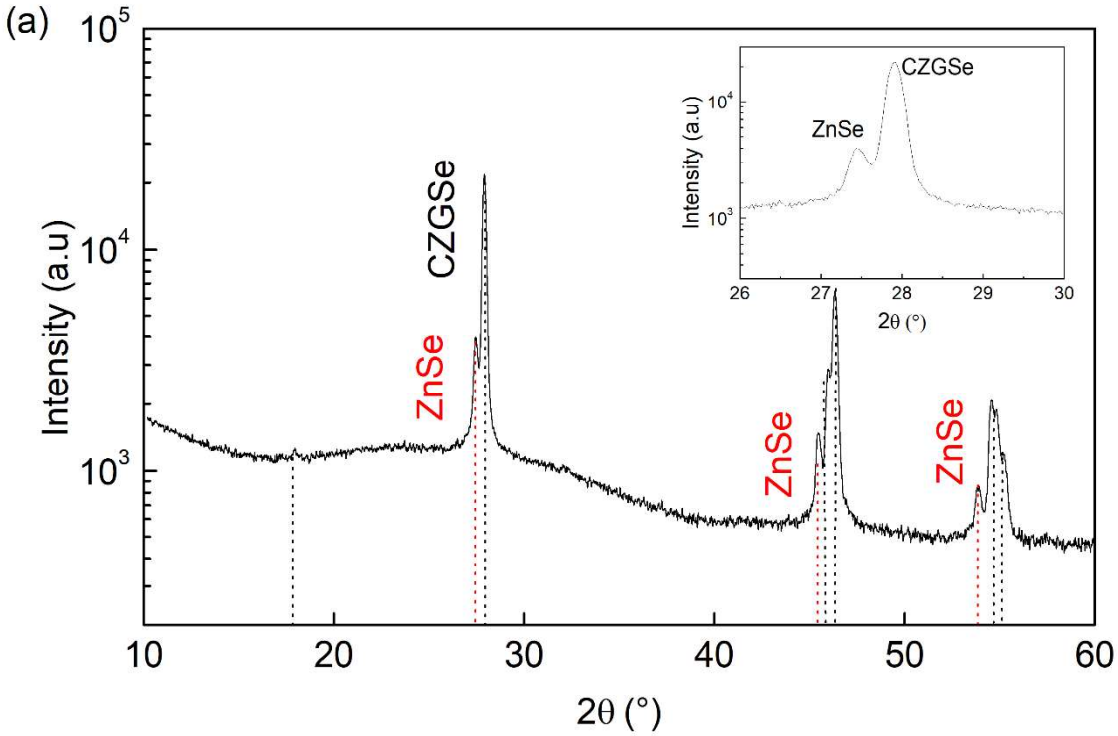

Figure 1(b)

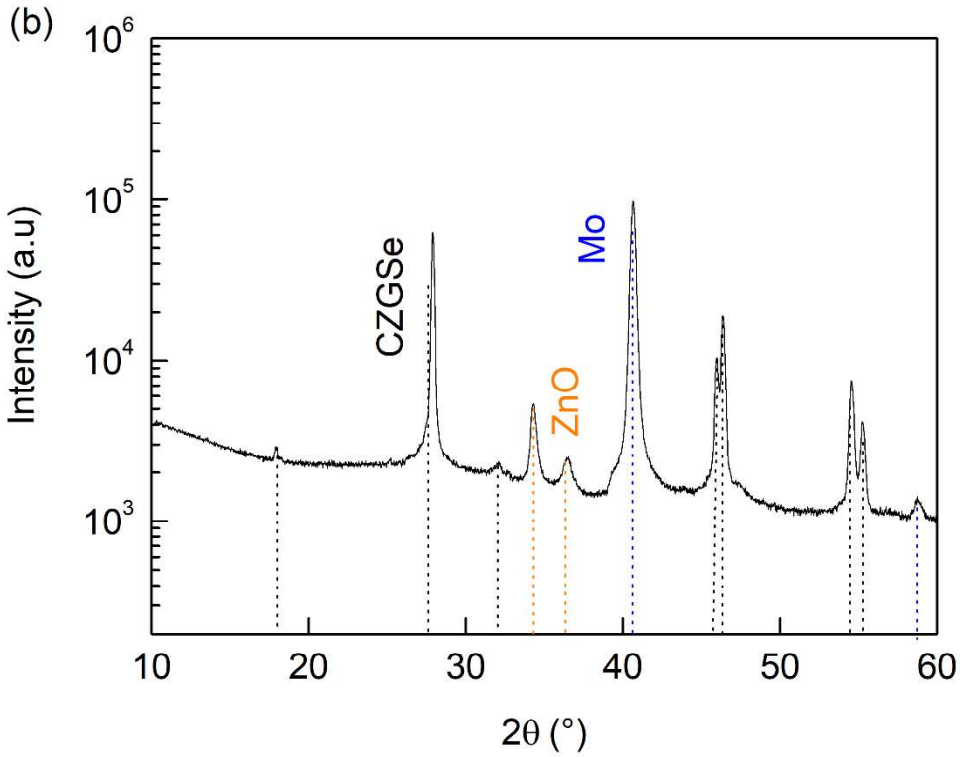

Figure 2

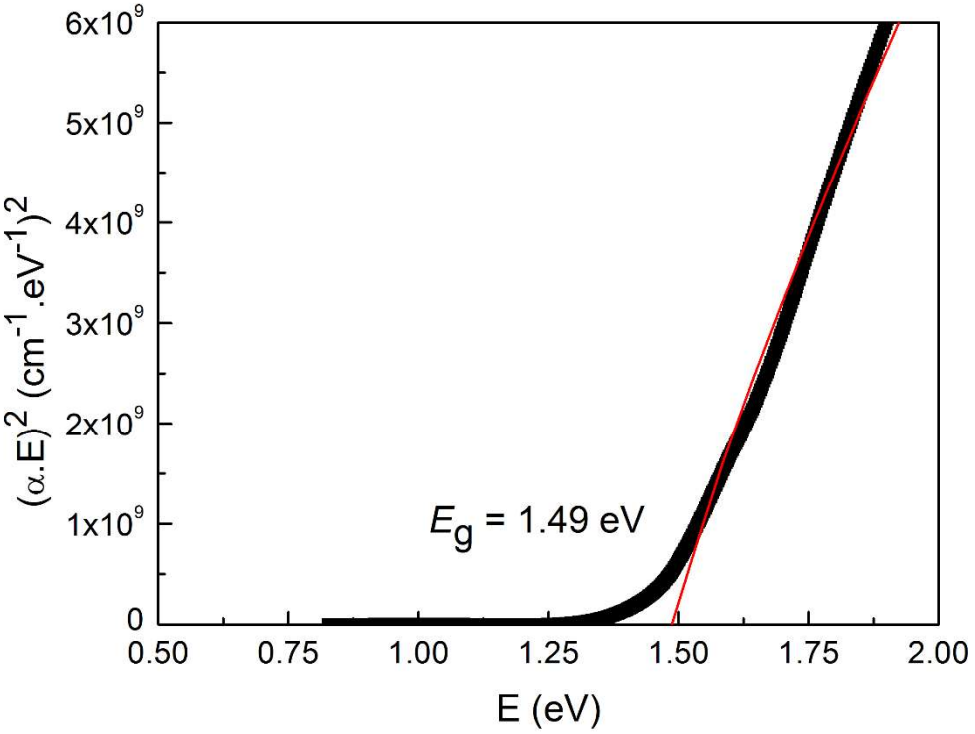

Figure 3

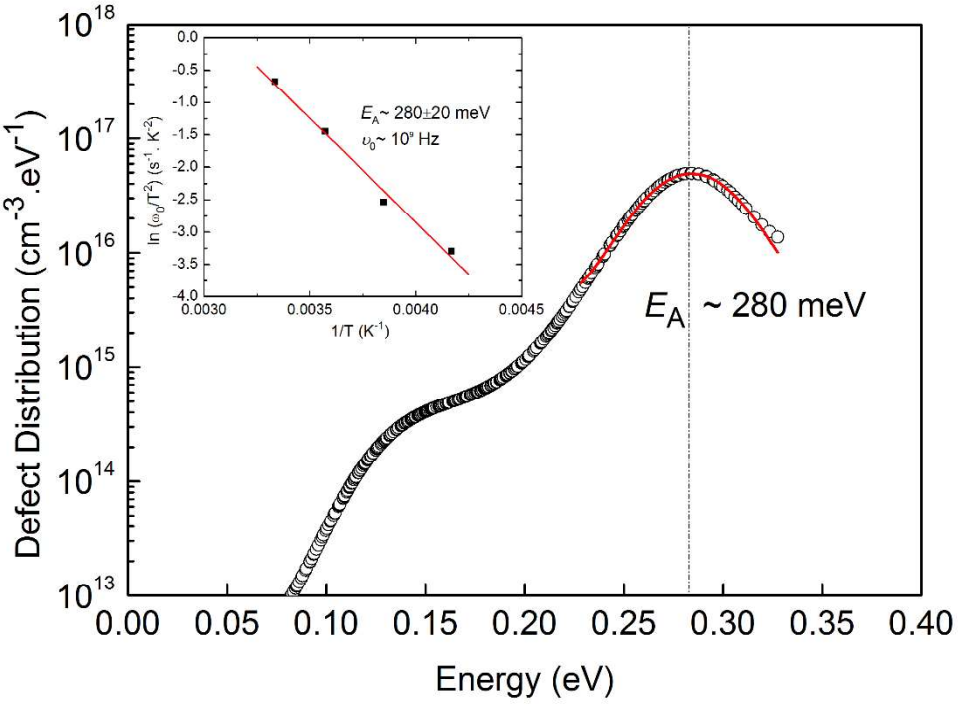

Figure 4

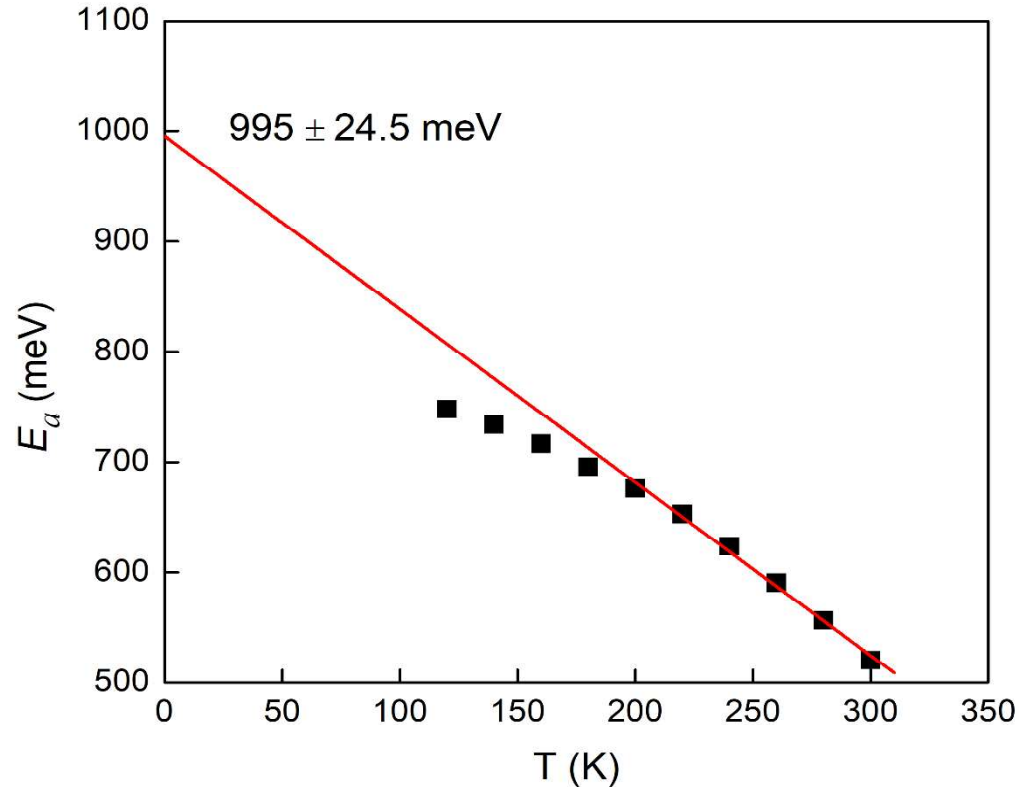

Figure 5

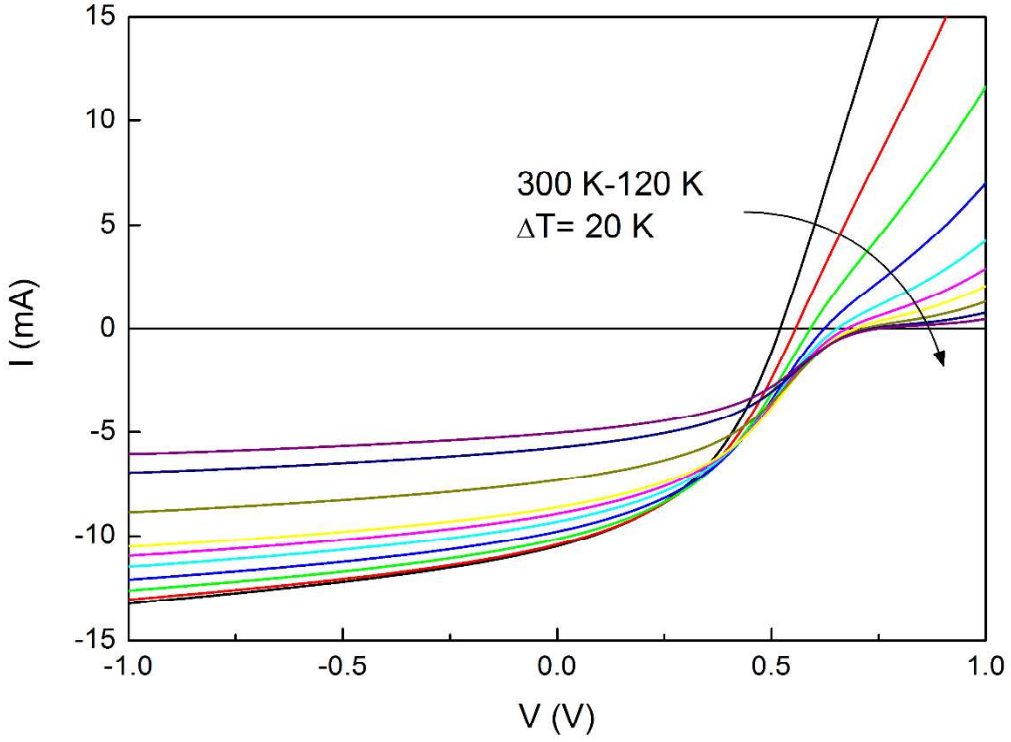

Figure 6

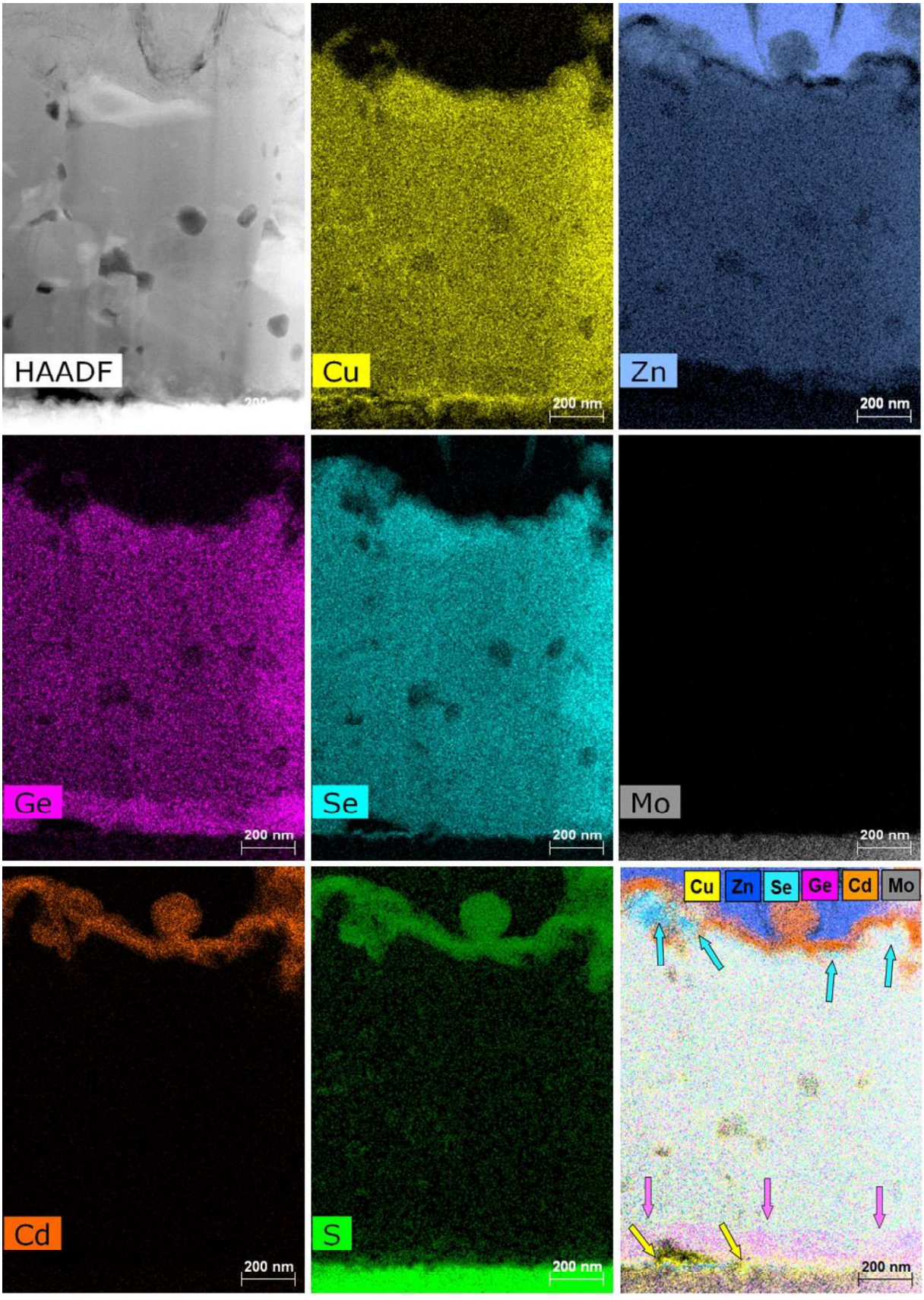
HAADF
Cu
200 nm
Zn
200 nm
Ge
200 nm
Se
200 nm
Mo
200 nm
Cd
200 nm
S
200 nm
Cu Zn Se Ge Cd Mo
200 nm

Figure 7

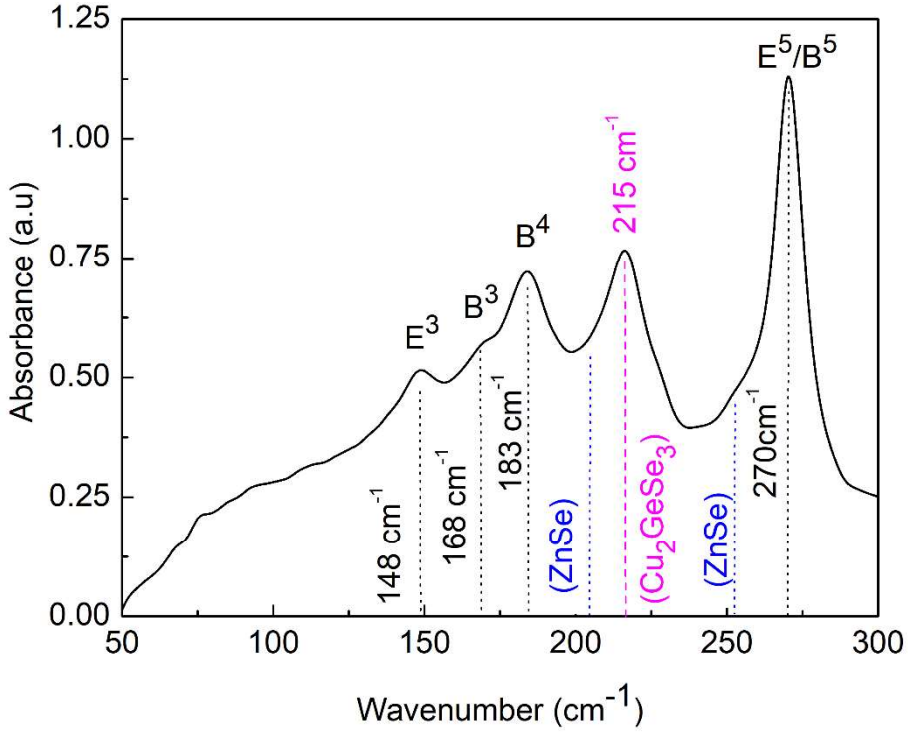

Figure 8

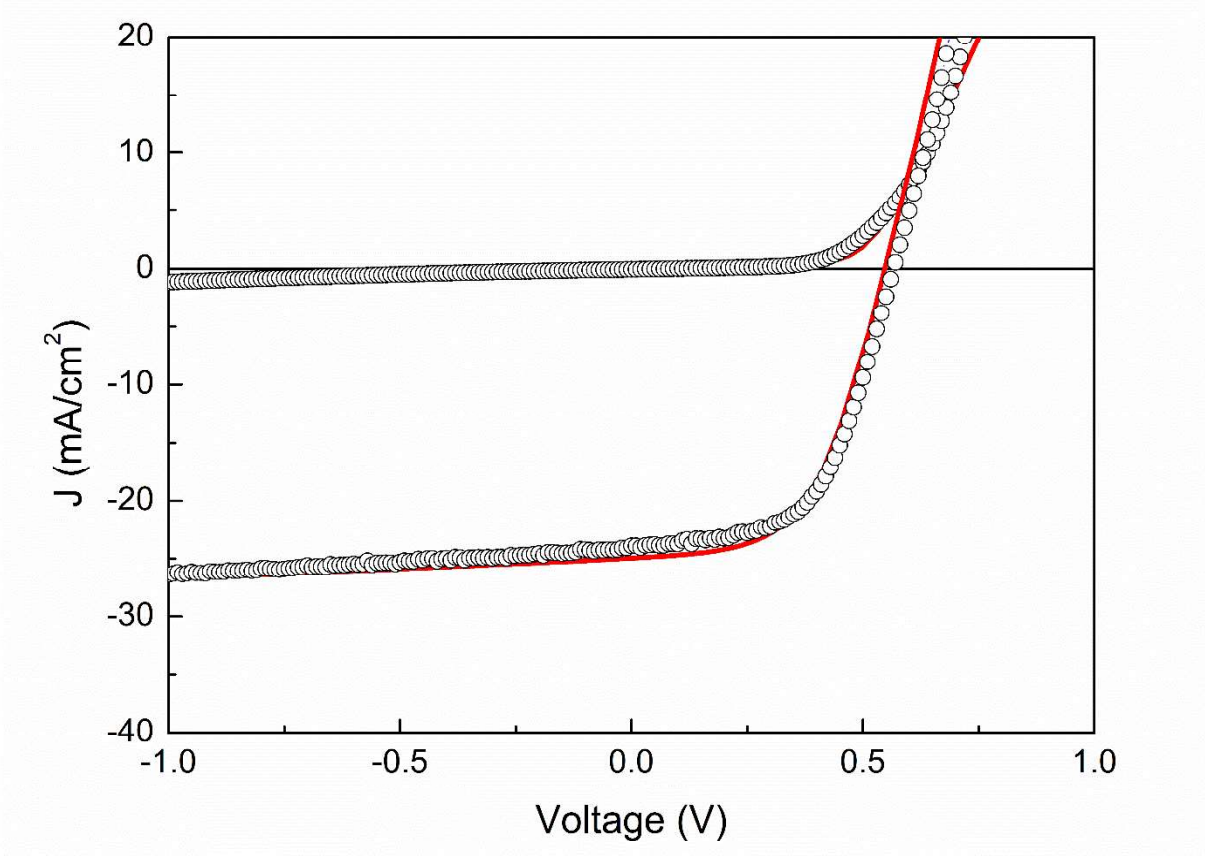

Figure 9 (a)

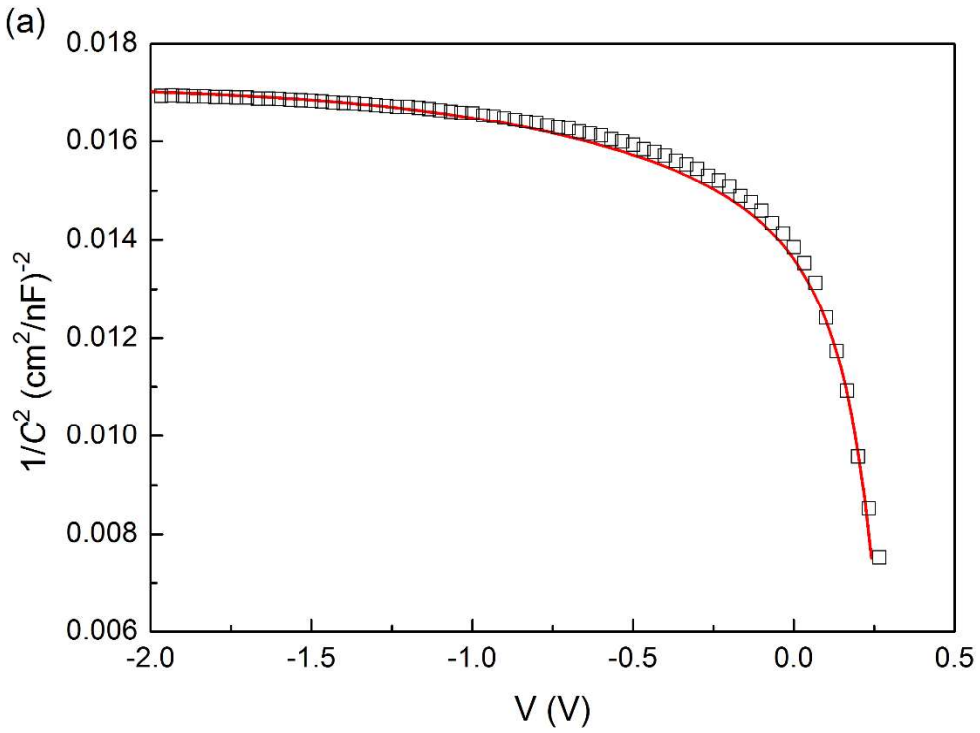

Figure 9 (b)

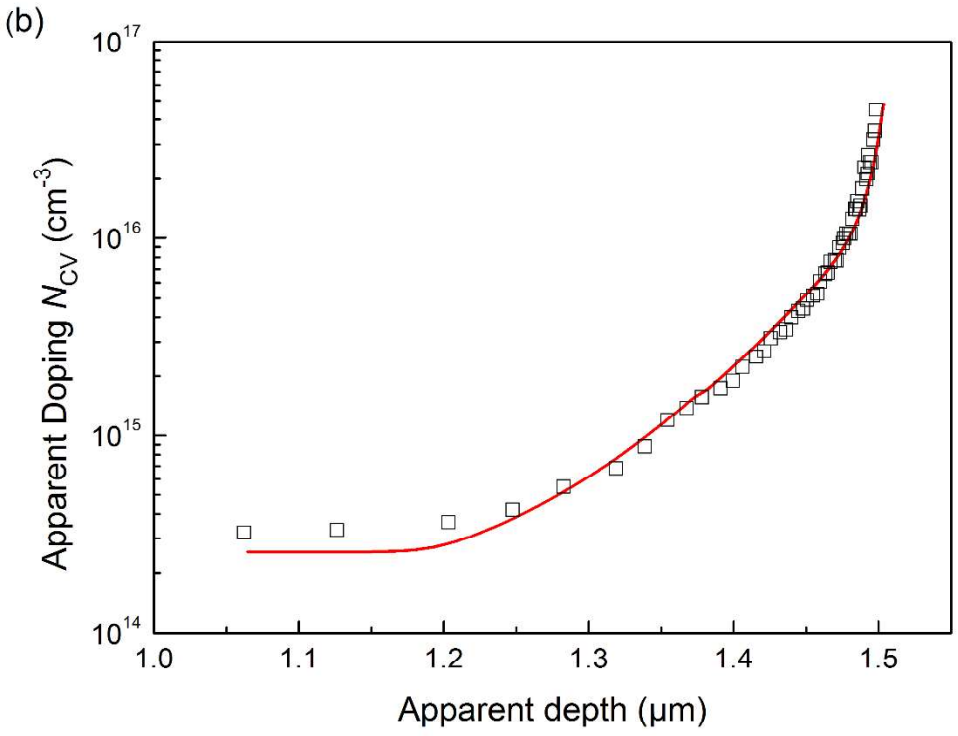

Figure 10

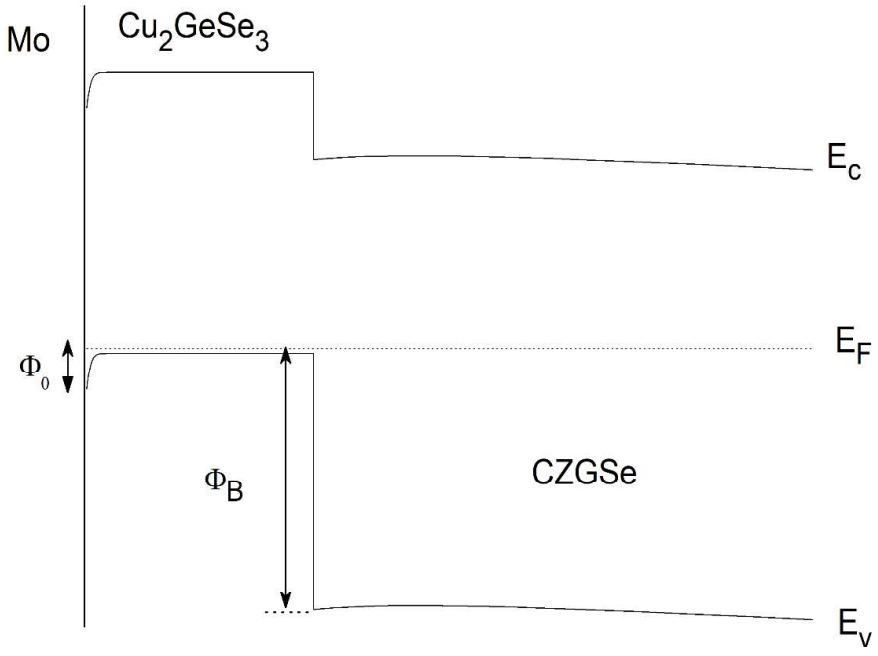

Figure 11 (a)

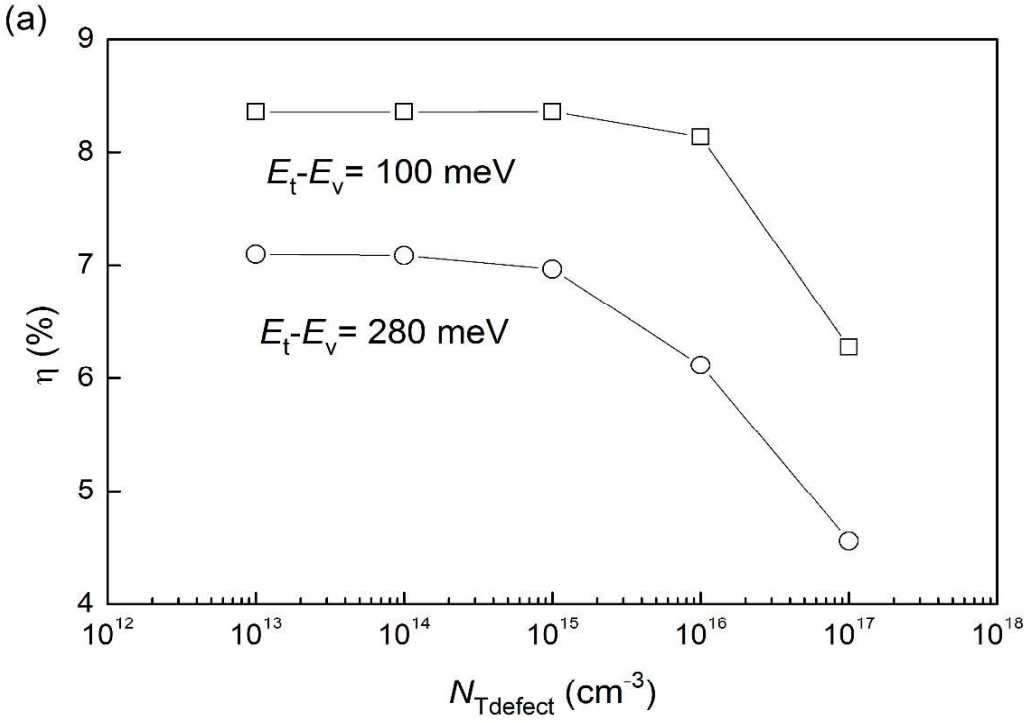

Figure 11 (b)

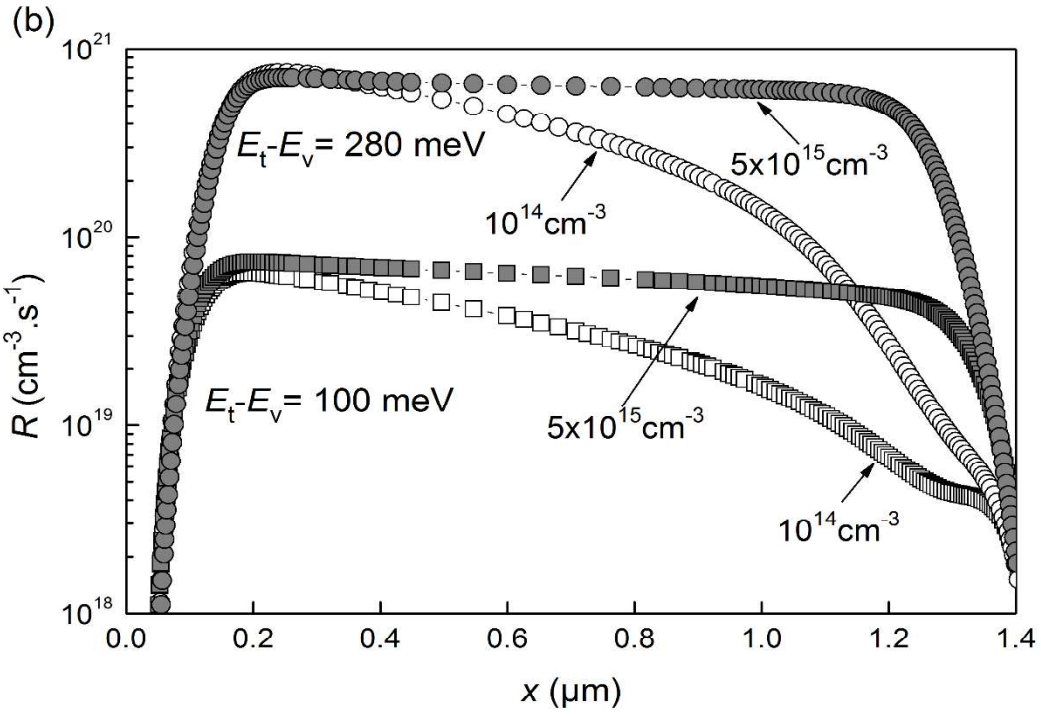

Figure 12(a)

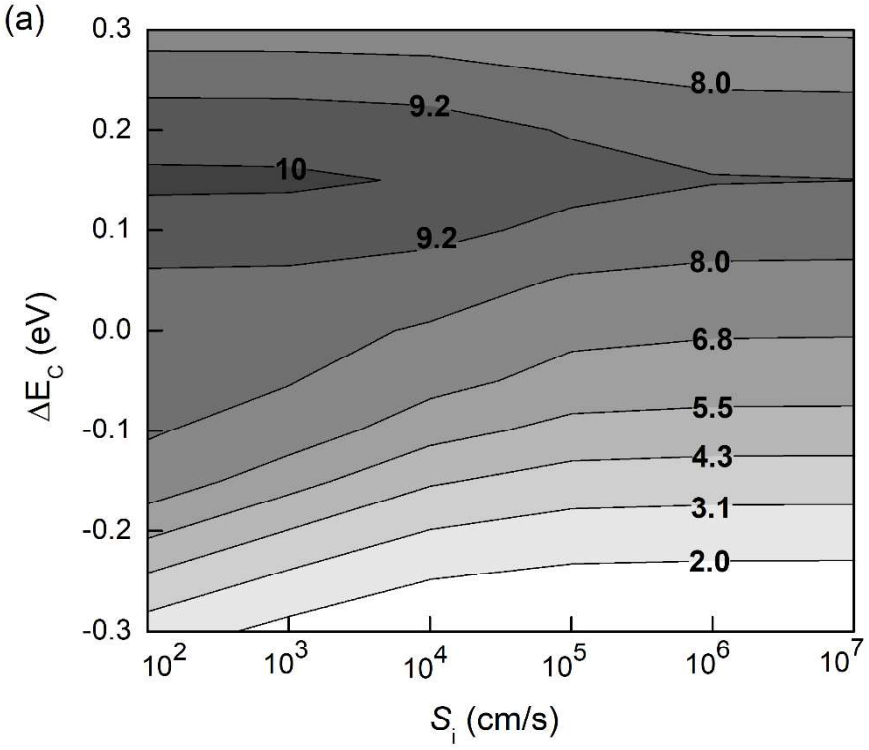

Figure 12(b)

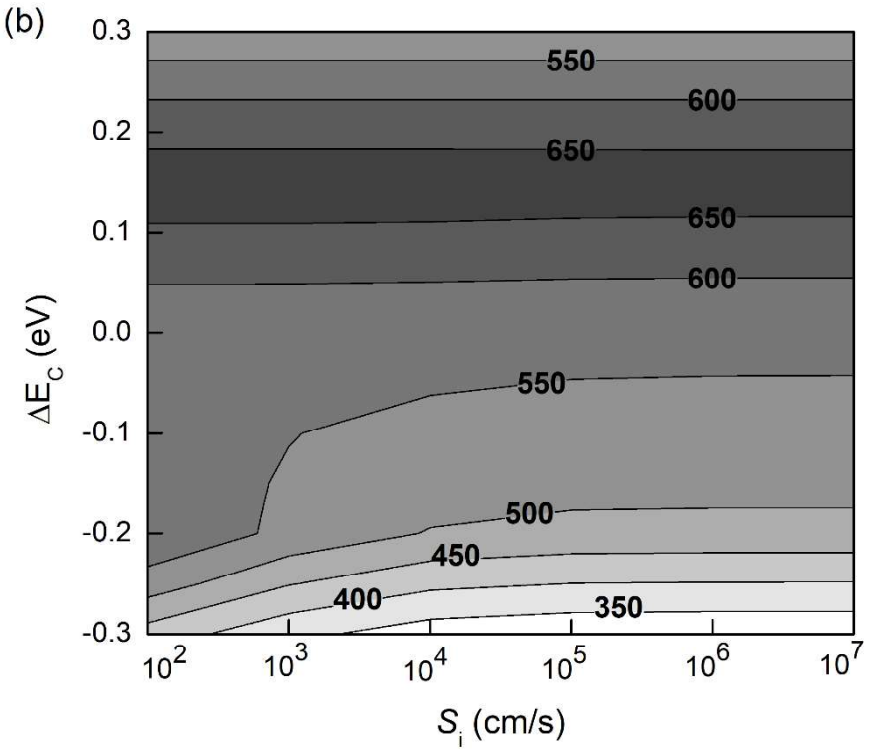

Figure 13

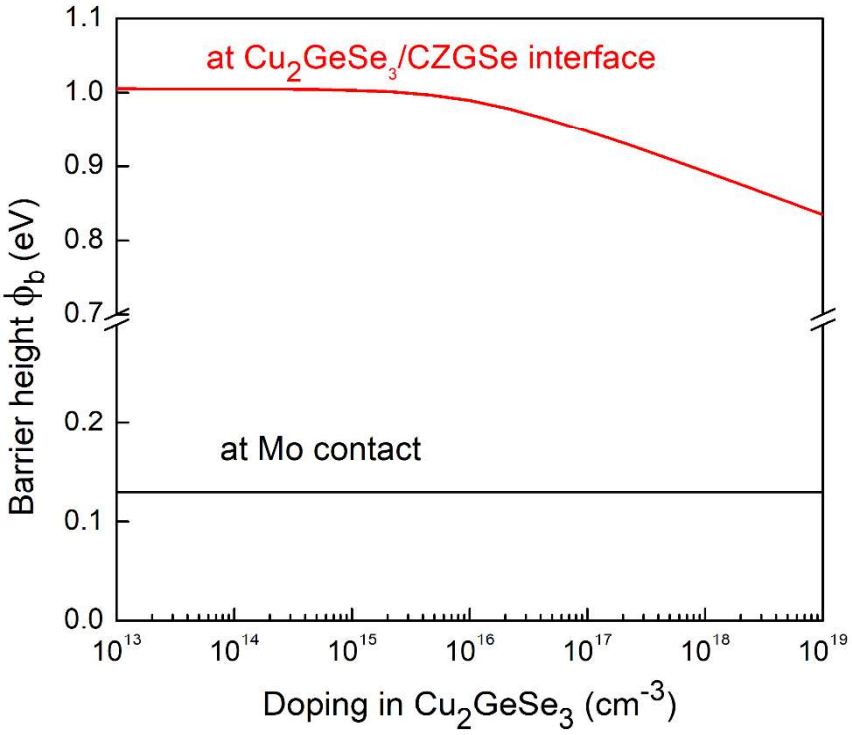

Figure 14

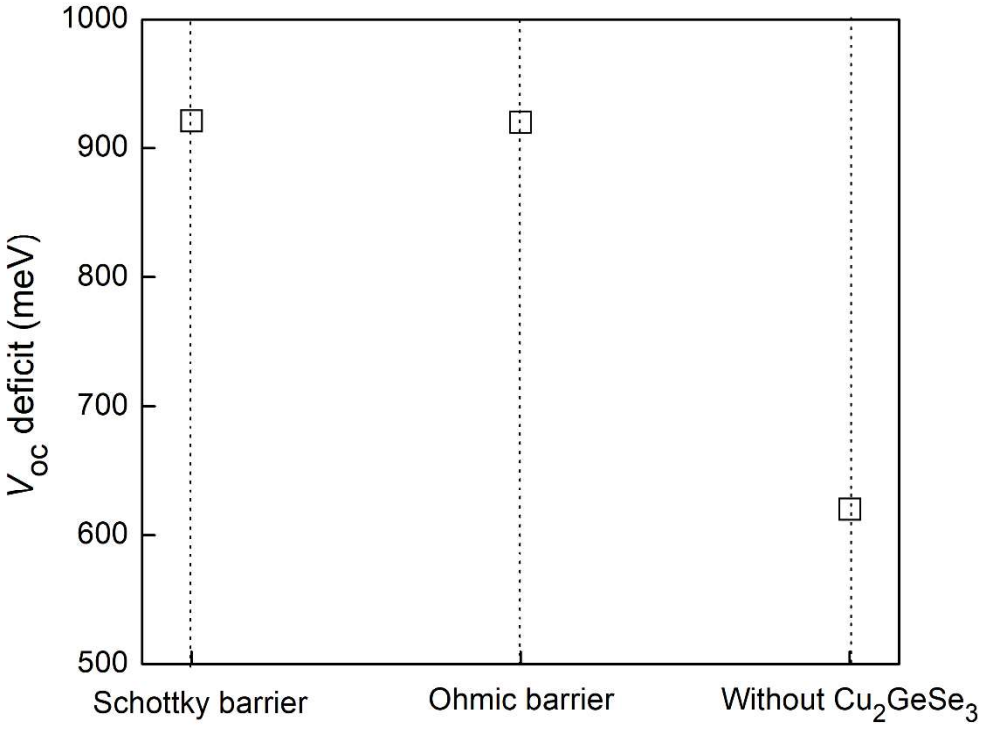

Figure 15

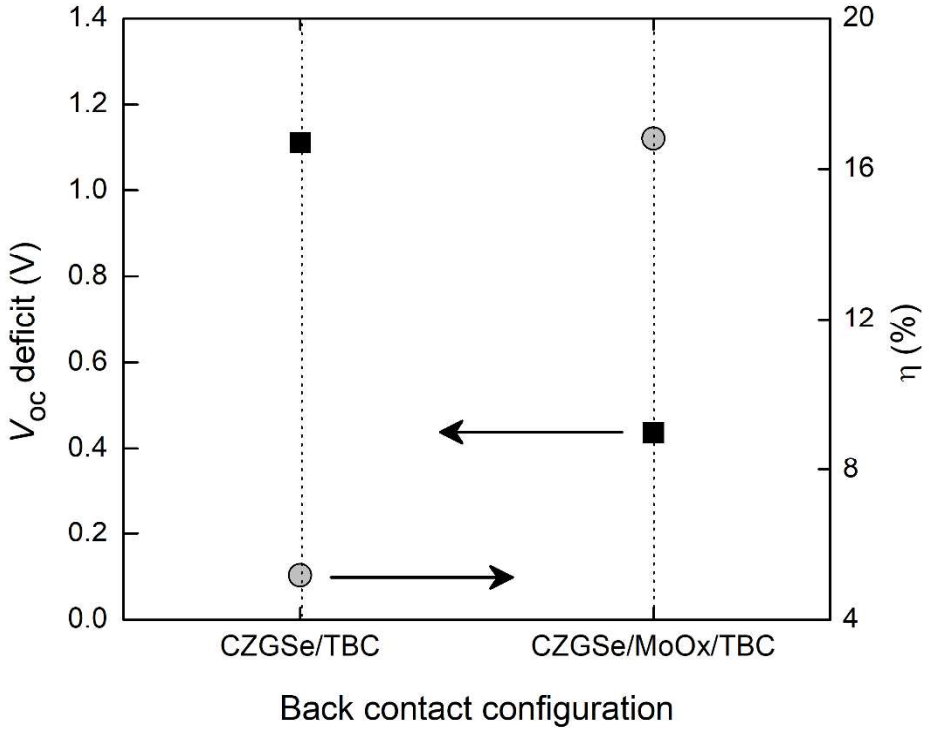

Figure 16

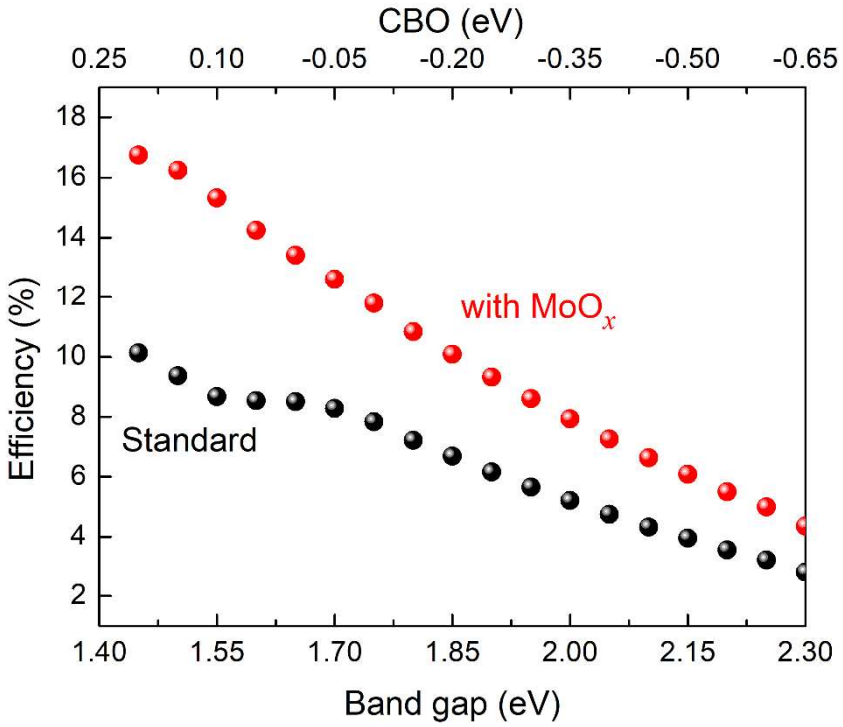

Figure 17 (a)

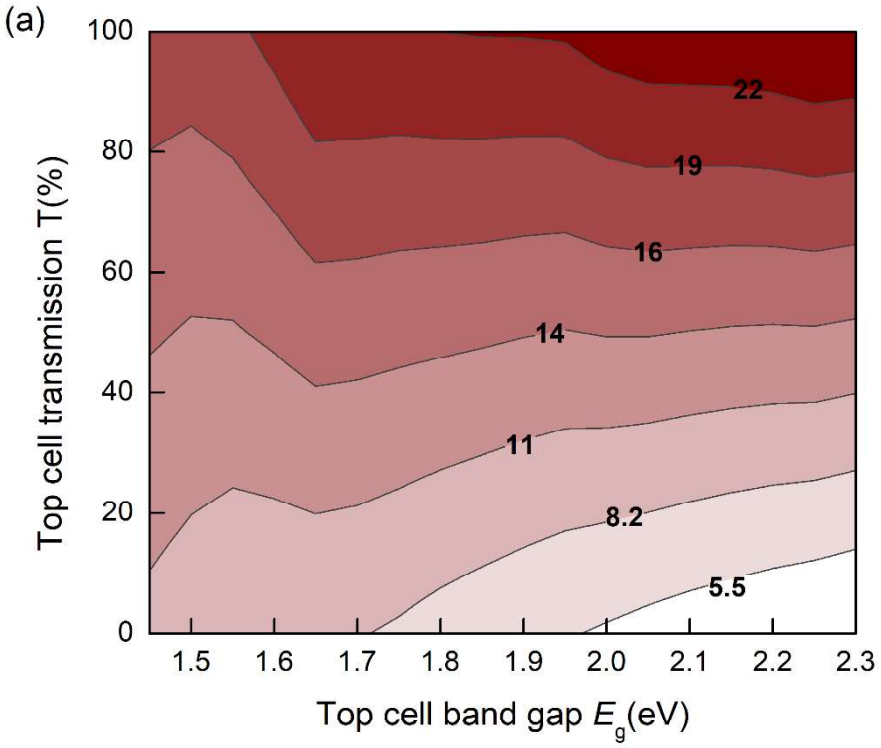

Figure 17 (b)

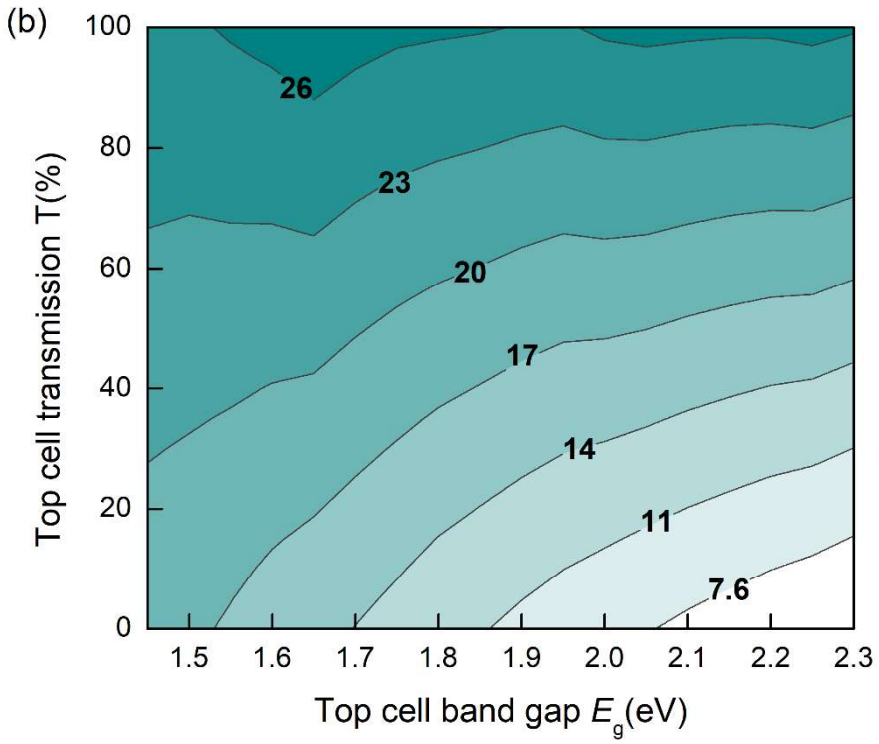

Figure 18

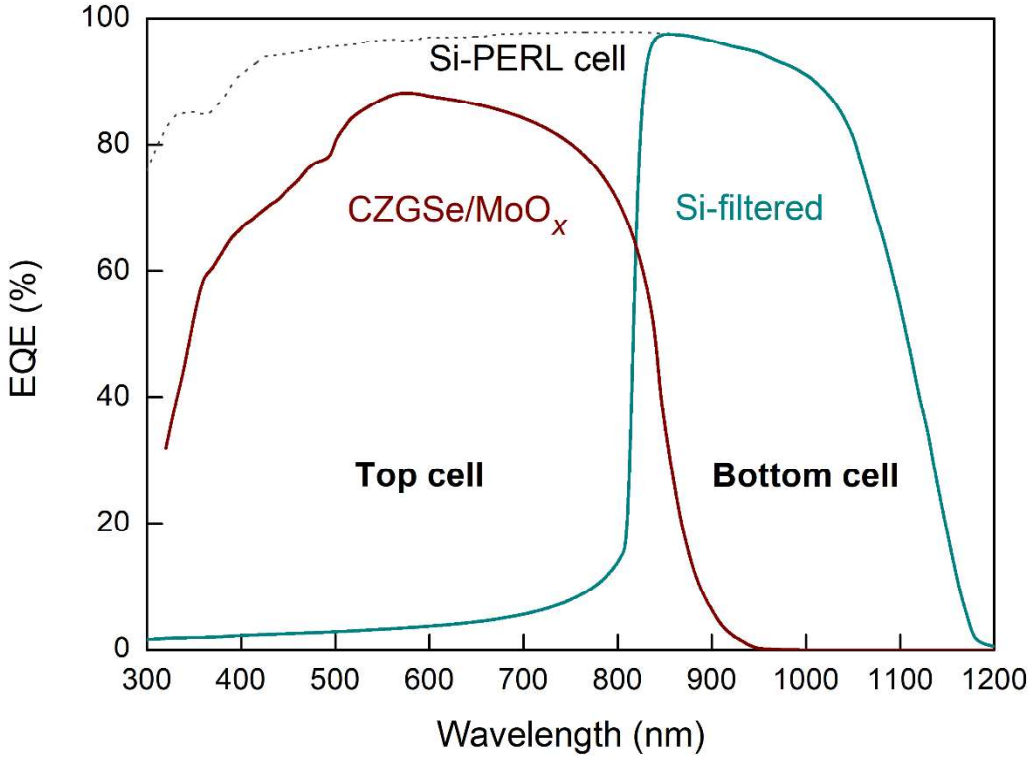

SUPPLEMENTARY INFORMATION FOR

The path towards efficient wide bandgap thin-film Kesterite solar cell with transparent back contact for viable tandem application

Samira Khelifi[a,b,*], Guy Brammertz[c,d,e], Léo Choubrac[f,h], Maria Batuk[g], Sheng Yang[a], Marc Meuris[c,d,e], Nicolas Barreau[f], Joke Hadermann[g], Henk Vrielinck[b], Dirk Poelman[b], Kristiaan Neyts[a], Bart Vermang[c,d,e], Johan Lauwaert[a]

[a] Department of Electronics and Information Systems (ELIS), Ghent University, iGhent Tower, Technology Park Zwijnaarde 126, 9052 Ghent, Belgium

[b] Department of Solid State Sciences, Ghent University, Krijgslaan S-1, 9000 Ghent, Belgium

[c] imec division IMOMEC-partner in Solliance, Wetenschapspark 1, 3590 Diepenbeek, Belgium

[d] Hasselt University-partner in Solliance, Martelarenlaan 42, 3500 Hasselt, Belgium

[e] EnergyVille, Thorpark 8320, 3600 Genk, Belgium

[f] Institut des matériaux Jean Rouxel (IMN), Université de Nantes, CNRS, 2 rue de la Houssiere, BP 32229, 44322 Nantes Cedex 03, France

[g] Electron Microscopy for Materials Science (EMAT), University of Antwerp, Groenenborgerlaan 171, 2020 Antwerp, Belgium.

[h] Department Structure and Dynamics of Energy Materials, Helmoltz-Zentrum Berlin für Materialien und Energie, Berlin 14109, Germany.

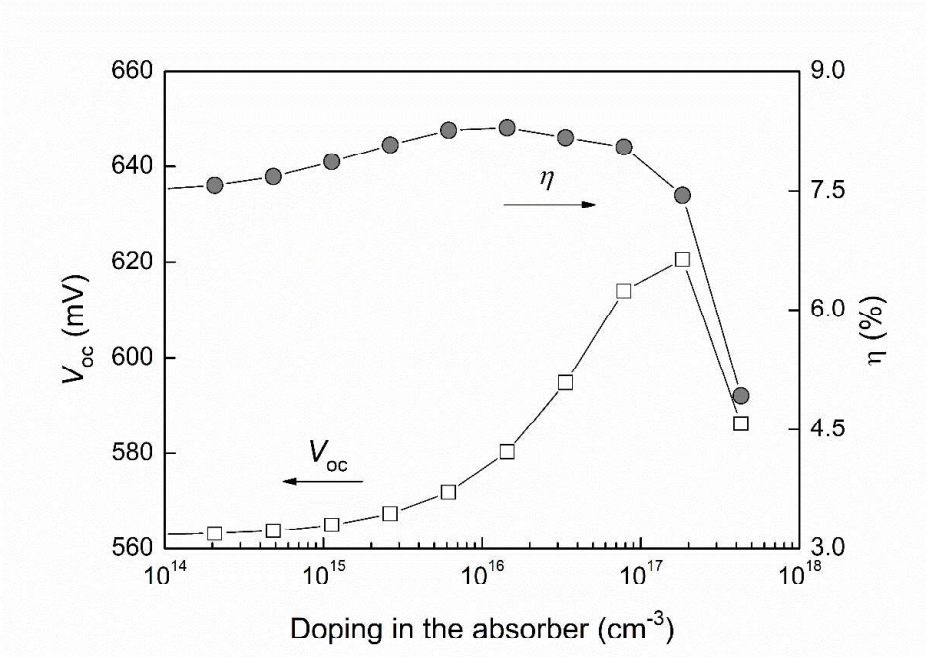

Figure S1: Effect of *p*-type doping in the CZGSe absorber on the open-circuit (V_{oc}) voltage and efficiency of the solar cell.

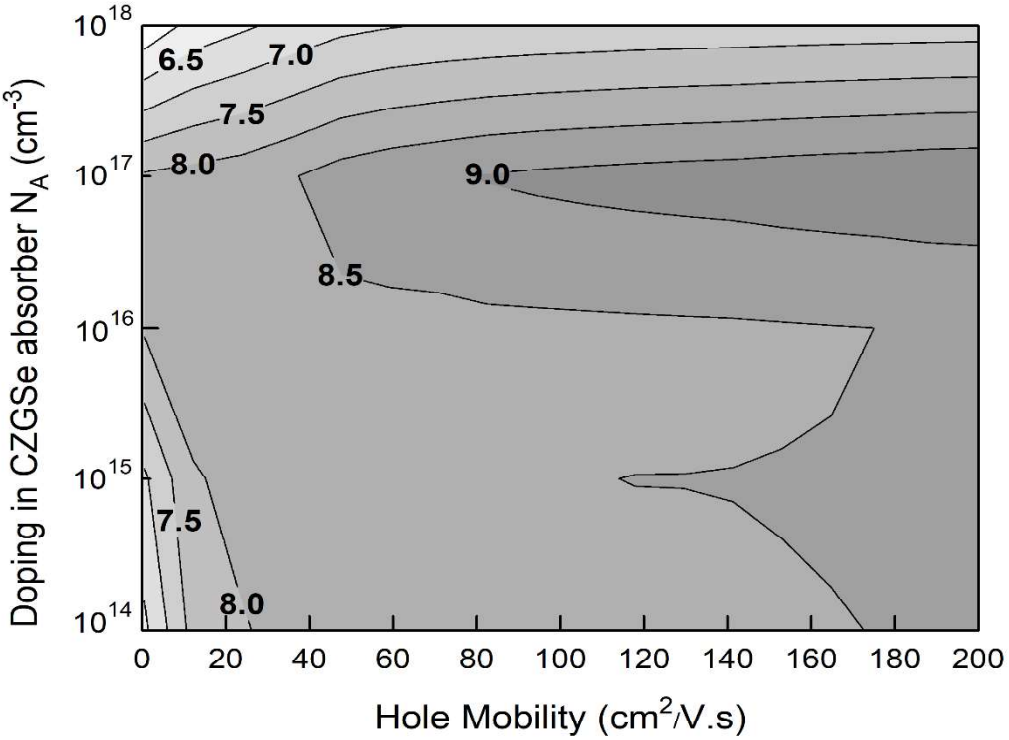

Figure S2: Efficiency (η) as a function of the doping and the hole mobility of the CZGSe absorber.

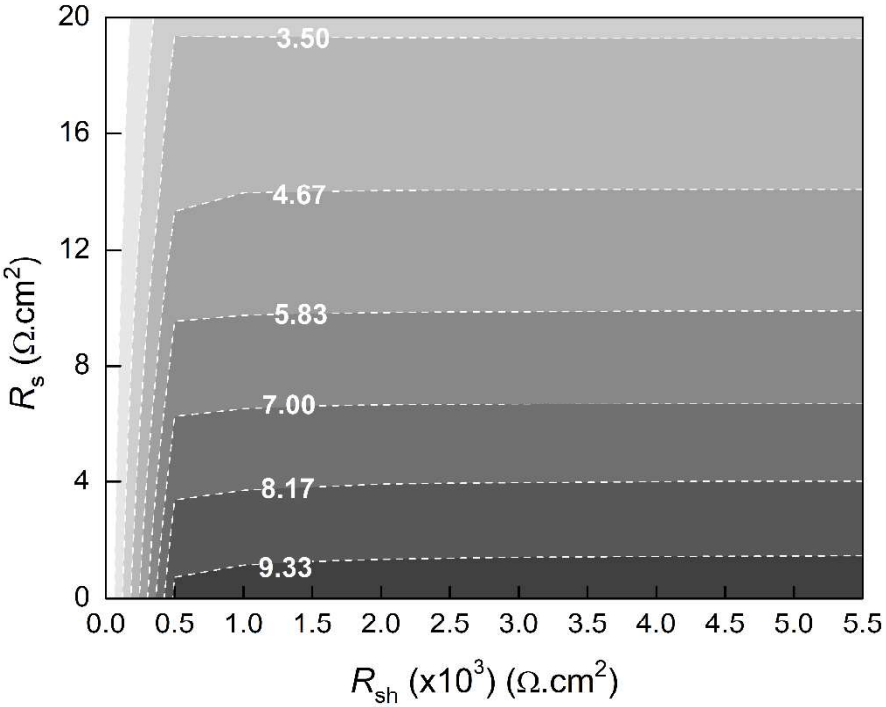

Figure S3: Effect of parasitic resistances series and shunt on the efficiency of the CZGSe solar cell

Table S1: Calculated and measured solar cell outputs of the CZGSe cell at standard conditions T=300K and A.M 1.5.

Solar cell output	Measurements	Simulations
Open-circuit voltage V_{oc} (mV)	560	555
Short-circuit current J_{sc} (mA/cm^2)	23.9	24.9
Fill Factor *FF* (%)	56.7	55
Efficiency η (%)	7.6	7.54

Declaration of interests

☒ The authors declare that they have no known competing financial interests or personal relationships that could have appeared to influence the work reported in this paper.

☐The authors declare the following financial interests/personal relationships which may be considered as potential competing interests:
